

The GNAT method for nonlinear model reduction: effective implementation and application to computational fluid dynamics and turbulent flows

Kevin Carlberg^{a,*}, Charbel Farhat^{b,**}, Julien Cortial^{a,*}, David Amsallem^{b,**}

^a*Sandia National Laboratories*

^b*Stanford University*

Abstract

The Gauss–Newton with approximated tensors (GNAT) method is a nonlinear model reduction method that operates on fully discretized computational models. It achieves dimension reduction by a Petrov–Galerkin projection associated with residual minimization; it delivers computational efficiency by a hyper-reduction procedure based on the ‘gappy POD’ technique. Originally presented in Ref. [1], where it was applied to implicit nonlinear structural-dynamics models, this method is further developed here and applied to the solution of a benchmark turbulent viscous flow problem. To begin, this paper develops global state-space error bounds that justify the method’s design and highlight its advantages in terms of minimizing components of these error bounds. Next, the paper introduces a ‘sample mesh’ concept that enables a distributed, computationally efficient implementation of the GNAT method in finite-volume-based computational-fluid-dynamics (CFD) codes. The suitability of GNAT for parameterized problems is highlighted with the solution of an academic problem featuring moving discontinuities. Finally, the capability of this method to reduce by orders of magnitude the core-hours required for large-scale CFD computations, while preserving accuracy, is demonstrated with the simulation of turbulent flow over the Ahmed body. For an instance of this benchmark problem with over 17 million degrees of freedom, GNAT outperforms several other nonlinear model-reduction methods, reduces the required computational resources by more than two orders of magnitude, and delivers a solution that differs by less than 1% from its high-dimensional counterpart.

Keywords: nonlinear model reduction, GNAT, gappy POD, CFD, mesh sampling

1. Introduction

Computational fluid dynamics (CFD) modeling and simulation tools have become indispensable in many engineering applications due to their ability to enhance the understanding of complex fluid systems, reduce design costs, and improve the reliability of engineering systems. Unfortunately, many desired high-fidelity CFD simulations are so computationally intensive that they can require unaffordable computational resources or time to completion, even when supercomputers with thousands of cores are available. Consequently, such simulations are often impractical for time-critical applications such as flow control, design optimization, uncertainty quantification, and system identification.

Projection-based nonlinear model-reduction methods constitute a promising approach for bridging the gap between CFD and such applications. These methods approximate a given high-fidelity model by reducing its dimension, i.e., the number of equations and unknowns that describe it. For this purpose, such methods

*7011 East Ave, MS 9159, Livermore, CA 94550. Sandia is a multiprogram laboratory operated by Sandia Corporation, a Lockheed Martin Company, for the United States Department of Energy under contract DE-AC04-94-AL85000.

**Durand Building, 496 Lomita Mall, Stanford University, Stanford, CA 94305-3035

Email addresses: ktcarlb@sandia.gov (Kevin Carlberg), cfarhat@stanford.edu (Charbel Farhat), jcortia@sandia.gov (Julien Cortial), amsallem@stanford.edu (David Amsallem)

URL: sandia.gov/~ktcarlb (Kevin Carlberg)

first perform intensive large-scale computations ‘offline’ to construct *a priori* a low-dimensional subspace onto which they project the high-dimensional model of interest. This leads to a reduced-order model (ROM) characterized by low-dimensional operators. Then, in an ‘online’ stage, they exploit this ROM to compute approximate solutions that lie in this pre-computed subspace.

Unfortunately, the computational cost associated with assembling the ROM’s low-dimensional operators — matrices and vectors for implicit schemes, and vectors for explicit ones — scales with the large dimension of the underlying high-dimensional model. For this reason, projection-based model-reduction methods are efficient primarily for problems where the aforementioned operators must be constructed only once, or can be assembled *a priori*. These include linear time-invariant systems [2, 3], linear stationary systems whose operators are affine functions of the input parameters [4, 5], and a class of nonlinear systems characterized by quadratic nonlinearities [6, 7, 8]. Within these contexts, projection-based model-reduction methods have been successfully applied to problems in structural dynamics [3], aerodynamics [9, 10, 11, 12, 13] and aeroelasticity [14, 15, 16, 17, 18, 19], among others.

On the other hand, when projection is applied to linear time-varying systems, linear stationary systems with nonaffine parameter dependence, or general nonlinear problems, the resulting ROM is costly to assemble. This high cost arises from the need to evaluate the high-dimensional nonlinear function (and possibly its Jacobian) at each computational step of a solution algorithm. To overcome this roadblock, several approaches have been proposed. Such complexity-reduction techniques are sometimes referred to as hyper-reduction methods [20, 21]. Several of these techniques are outlined below.

The ‘empirical interpolation’ method developed for linear elliptic problems with non-affine parameter dependence [22], as well as for nonlinear elliptic and parabolic problems [23], reduces the computational cost associated with nonlinearities by interpolating the governing nonlinear function at a few spatial locations using an empirically derived basis. This method operates directly on the governing partial differential equation (PDE) and therefore at the continuous level. Its variant proposed in Ref. [24] relies for the same purpose on ‘best [interpolation] points’ and a POD basis. The hyper-reduction method proposed in Ref. [25, 26] extends the empirical-interpolation method to the case of a scalar conservation law discretized by an explicit solution algorithm. However, no further extension of this method to CFD has been performed, as this is not a straightforward task.

Alternatively, the trajectory piece-wise linear (TPWL) method developed in [27] operates at the semi-discrete level, i.e., on the ordinary differential equation (ODE) obtained after discretizing the PDE in space. TPWL constructs a ROM as a weighted combination of linearized models, where each linearization point lies on a training trajectory. However, because the resulting ROM never queries the underlying high-dimensional model away from the linearization points, this method in principle lacks robustness for highly nonlinear problems such as those arising from a large class of CFD applications.

Another class of hyper-reduction methods reduces computational complexity by computing only a few entries of the nonlinear function (and possibly its Jacobian) appearing in the governing ODE. In this paper, such methods are referred to as function-sampling methods; these methods also operate at the semi-discrete level. They include collocation approaches, which compute a small subset of the entries of the residual vector. Ref. [28] proposes collocation of the nonlinear equations followed by a least-squares solution of the resulting overdetermined system of nonlinear equations. Similarly, Refs. [29, 20] propose a collocation of the equations followed by a Galerkin projection. Function-reconstruction approaches define another subset of function-sampling methods. In contrast to collocation methods, these techniques use the sampled entries of the nonlinear function to approximate the entire nonlinear function by interpolation or least-squares regression. One such method reconstructs the governing nonlinear function in the least-squares sense, using the same basis adopted to represent the state. This approach was developed in for parameter-varying systems [29]¹ and for nonlinear dynamical systems discretized by explicit time-integration schemes [30]. Other function-reconstruction approaches include the semi-discrete analogs to the empirical and best points interpolation methods that have been developed for parameterized nonlinear stationary problems [31, 32], and for nonlinear

¹For such problems, this method is mathematically equivalent to collocation followed by a Galerkin projection when the resulting overdetermined system is solved by a Galerkin projection method.

dynamics problems [31, 33].

Although some of the function-reconstruction methods outlined above have been successfully applied to large-scale steady-state problems (e.g., see Ref. [32]), it will be shown that many of them lack the robustness needed to address highly nonlinear dynamical systems such as those arising from unsteady CFD applications.

The Gauss–Newton with approximated tensors (GNAT) method [1] is a nonlinear Petrov–Galerkin projection method equipped with a function-sampling hyper-reduction scheme. In contrast with the aforementioned nonlinear model-reduction methods, it operates at the discrete level, i.e., on the system of nonlinear equations arising at each time step, which is obtained after discretizing the PDE in both space and time. GNAT is designed around approximations that satisfy consistency and discrete-optimality conditions. As such, it has been successfully applied to nonlinear structural-dynamics problems [1] for which it demonstrated robustness, accuracy, and excellent CPU performance.

This work further develops the GNAT methodology and demonstrates its potential for CFD applications. Section 2 formulates the problem of interest, and Section 3 provides an overview of GNAT. Within this overview, a new consistent snapshot-collection procedure is proposed in Section 3.3.2. Next, Section 4 presents global error bounds for the discrete fluid state in the case of the implicit backward-Euler scheme. This time integrator may be of little practical importance to CFD, but the developed error bounds highlight the merits of the principles underlying the construction of a GNAT ROM. Then, Section 5 proposes a simple yet effective implementation of GNAT’s online stage on parallel computing platforms. This implementation features the concept of a ‘sample mesh’, which is a carefully chosen *tiny* subset of the original CFD mesh on which all online GNAT computations are performed. The sample mesh has few connectivity requirements and is therefore easily amenable to partitioning for parallel distributed computations. Most importantly, the implementation can be tailored to any specific CFD scheme or software, and to the fast computation of outputs such as pressure coefficients, lift, and drag. Section 6 demonstrates the potential of GNAT to effectively reduce the dimension and complexity of highly nonlinear CFD models while maintaining a high level of accuracy. In Section 6.1, GNAT is applied to a parameterized hyperbolic problem featuring a moving shock; GNAT’s online performance is tested for parameter values different from those used to collect simulation data offline. Section 6.2 demonstrates the potential of GNAT for challenging CFD applications with the fast solution of a benchmark turbulent flow problem with over 17 million unknowns. For this problem, GNAT outperforms many of the aforementioned nonlinear model-reduction methods. It reproduces the solution delivered by the high-dimensional CFD model with less than 1% discrepancy, while reducing the associated computational cost in core-hours by more than two orders of magnitude. Finally, Section 7 offers conclusions.

2. Problem formulation

2.1. Parameterized nonlinear CFD problem

Consider the ODE resulting from semi-discretizing the conservation form of the compressible Navier–Stokes equations by a finite difference, finite volume, or stabilized finite element method — possibly augmented by a turbulence model — and a given set of boundary conditions:

$$\begin{aligned}\frac{dw}{dt} &= F(w(t), t; \mu) \\ w(0) &= w^0(\mu).\end{aligned}\tag{1}$$

Let

$$\begin{aligned}z &= H(w(t), \mu) \\ &= L(\mu)\end{aligned}\tag{2}$$

denote the outputs of interest that may include the lift, drag, and other quantities.

Here, $t \in \mathbb{R}^+$ denotes time, $w \in \mathbb{R}^N$ denotes the discrete fluid state vector (i.e., the vector of discrete conserved fluid variables), N designates the dimension of the semi-discretization and is typically large,

$w^0 : \mathbb{R}^d \rightarrow \mathbb{R}^N$ denotes the parameterized initial condition, and $F : \mathbb{R}^N \times \mathbb{R}^+ \times \mathbb{R}^d \rightarrow \mathbb{R}^N$ is the nonlinear function arising from the semi-discretization of the convective and diffusive fluxes and source term (when present). The d input parameters, which may include shape parameters, free-stream conditions, and other design or analysis parameters of interest, are denoted by $\mu \in \mathbb{R}^d$. The (feasible) input-parameter domain is denoted by \mathcal{D} , and therefore $\mu \in \mathcal{D} \subset \mathbb{R}^d$. $H : \mathbb{R}^N \times \mathbb{R}^d \rightarrow \mathbb{R}^p$ and $L : (\mu) \mapsto H(w(t; \mu), \mu)$ define two equivalent mappings for the output vector $z \in \mathbb{R}^p$.

In this work, attention is occasionally focused on a finite-volume semi-discretization method operating on a dual CFD mesh. Consequently, the sampling concepts discussed in Sections 3 and 5 are node/cell oriented. However, all concepts, algorithms, and techniques presented in this paper are easily extendible to finite-difference and stabilized finite-element semi-discretization methods.

2.2. Objective: time-critical analysis

Consider the following objective: given inputs $\check{\mu} \in \mathcal{D}$, compute fast approximations of the outputs $\tilde{L}(\check{\mu}) \approx L(\check{\mu})$, where “fast” is defined in one of the following senses:

1. The evaluation takes a sufficiently small amount of *time*. This is relevant to applications that demand near-real-time analysis, where the objective is to compute outputs in a time below a threshold value; the number of computational cores required to perform the analysis is not a primary concern. Examples include flow control and routine analysis, where the analyst may require an answer within a given time frame.
2. The evaluation consumes a sufficiently small amount of *computational resources*, as measured by computational cores multiplied by time. This is relevant to many-query applications, where the objective is to evaluate the model at as many points in the input space as possible, given a fixed amount of wall time and processors. Examples include aerodynamic shape optimization and uncertainty quantification.

When the number of degrees of freedom N of the high-dimensional CFD model is sufficiently large, solving the state equations (1) with $\mu = \check{\mu}$ and subsequently computing the outputs by Eq. (2) becomes prohibitively time- and resource-intensive for time-critical applications.

Instead, the following two-stage offline-online strategy can be employed. During the offline stage, Eq. (1) is solved for d_{train} points in the input-parameter domain; this defines the training domain $\mathcal{D}_{\text{train}} \equiv \{\mu^j\}_{j=1}^{d_{\text{train}}} \subset \mathcal{D}$. The data acquired during these training simulations are then used to construct a surrogate model that is capable of rapidly reproducing the behavior of the high-dimensional model at arbitrary points in \mathcal{D} . The online stage uses this surrogate model to perform time-critical analysis for inputs $\check{\mu}$ with $\check{\mu} \notin \mathcal{D}_{\text{train}}$ in general.

In contrast to surrogate-modeling techniques based on data-fit approximations (e.g., response surfaces) of the input-output map $L(\mu)$, model-reduction methods take a more physics-based approach. These techniques aim to achieve time-critical analysis by *approximately* solving the (physics-based) state equations for the online inputs $\check{\mu}$ and then computing the resulting outputs. The next section provides an overview of the GNAT model-reduction method developed for this purpose.

3. Overview of the GNAT model-reduction method

To keep this paper as self-contained as possible, this section provides an overview of the Gauss-Newton with approximated tensors (GNAT) nonlinear model-reduction method first proposed in Ref. [1].

3.1. Computational strategy and numerical properties

Nonlinear model reduction is often performed in a somewhat *ad hoc* manner. As a result, nonlinear ROMs often lack important numerical properties. To avoid this pitfall, the design of the GNAT method employs a computational strategy that constructs approximations to meet conditions related to notions of *discrete optimality* and *consistency*.

The design of GNAT is based on the premise that if a given computational model is unaffordable for a given time-critical application, approximations can be introduced to this model to make it more economical yet retain an appropriate level of accuracy. This premise leads to a hierarchy of models characterized by tradeoffs between accuracy and computational complexity. Then, the objective is to construct computationally efficient approximations that introduce minimal error with respect to the previous model in the hierarchy. GNAT achieves this objective by relying on the concepts of discrete optimality and consistency introduced in Ref. [1]. Both concepts are recalled below.

Discrete-optimal approximation: Here, an approximation is said to be discrete optimal if it leads to approximations that — at the discrete level — minimize an error measure associated with the previous model in the hierarchy. This ensures that some measure of the error in the discrete approximation decreases monotonically as the approximation spaces expand (a property also referred to as *a priori* convergence).

Consistent approximation: Here, an approximation is said to be consistent if, when implemented without snapshot compression, it introduces no additional error in the solution at the training inputs.

Figure 1 depicts the model hierarchy employed by GNAT. This hierarchy consists of three computational models: the original tier I high-dimensional model and two increasingly approximated models referred to as the tier II and tier III (reduced-order) models, respectively. Each of these reduced-order models is generated by 1) acquiring snapshots from simulations performed for training inputs $\mathcal{D}_{\text{train}}$ using the previous (i.e., more accurate) model in the hierarchy, 2) compressing the snapshots, and 3) introducing an approximation that exploits the compressed snapshots.

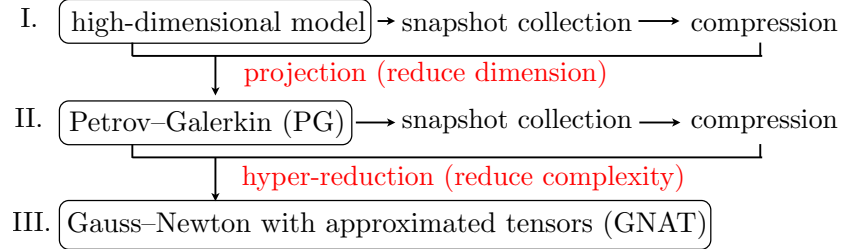


Figure 1 Model hierarchy with approximations shown in red.

3.2. Fully discrete computational framework

As stated in the introduction, GNAT operates at the discrete level. That is, the method introduces approximations after ODE (1) has been discretized in time. Hence, the ROM constructed by GNAT is a low-dimensional algebraic system that governs the solution of ODE (1) at each time step; it cannot generally be expressed as a low-dimensional ODE. As such, GNAT may be less convenient than other model reduction methods: the ROM it produces is valid only for the time-integrator adopted for the high-dimensional model. However, Section 3.3 will show that the fully discrete framework enables GNAT to achieve discrete optimality.

Throughout the remainder of this paper, it is assumed that Eq. (1) is solved by an implicit linear multi-step time integrator. In this case, if n_t time steps are carried out, a sequence of n_t systems of nonlinear equations arises. Each of these systems can be written as

$$R^n(w^{n+1}; \mu) = 0 \quad (3)$$

for $n = 0, \dots, n_t - 1$, with outputs

$$z = G(w^0, \dots, w^{n_t}, \mu). \quad (4)$$

Here, a superscript n designates the value of a variable at time step n , the operators $R^n : \mathbb{R}^N \times \mathbb{R}^d \rightarrow \mathbb{R}^N$ for $n = 0, \dots, n_t - 1$ are nonlinear in both arguments, and $G : \mathbb{R}^N \times \dots \times \mathbb{R}^N \times \mathbb{R}^d \rightarrow \mathbb{R}^p$. The fluid state

vectors w^n , $n = 1, \dots, n_t$ are implicitly defined by Eq. (3) for a given μ , and $w^0 = w^0(\mu)$ is given by the initial condition.

For simplicity, consider one instance of Eq. (3) defined by one time instance and one vector of input parameters. Such an instance can be written as

$$R(w) = 0. \quad (5)$$

Here, the fluid state vector $w \in \mathbb{R}^N$ is implicitly defined by Eq. (5), and $R : \mathbb{R}^N \rightarrow \mathbb{R}^N$ with $w \mapsto R(w)$ is a nonlinear mapping. In the remainder of this paper, Eq. (5) is associated with the high-dimensional CFD model (tier I in Figure 1).

3.3. Petrov–Galerkin projection

To reduce the dimension of Eq. (5), the GNAT method employs a projection process. This leads to the tier II ROM in the model hierarchy. Specifically, GNAT seeks an approximate solution \tilde{w} to Eq. (5) in the affine trial subspace $w^0 + \mathcal{W} \subset \mathbb{R}^N$ of dimension $n_w \ll N$. Hence, \tilde{w} can be written as

$$\tilde{w} = w^0 + \Phi_w w_r, \quad (6)$$

where $\Phi_w \in \mathbb{R}^{N \times n_w}$ is a matrix representing an n_w -dimensional basis for \mathcal{W} , and $w_r \in \mathbb{R}^{n_w}$ denotes the generalized coordinates of the fluid state vector in this basis. Note that the *increment* in the state $\tilde{w} - w^0$ and not the state itself is sought in the subspace \mathcal{W} . This is an important consideration when defining the basis Φ_w as will be described in Section 3.3.2.

3.3.1. Discrete optimality

Substituting Eq. (6) into Eq. (5) yields $R(w^0 + \Phi_w w_r) = 0$, which represents an overdetermined system of N equations in n_w unknowns. Consequently, the GNAT method computes \tilde{w} as the solution to the minimization problem

$$\underset{\bar{w} \in w^0 + \mathcal{W}}{\text{minimize}} \|R(\bar{w})\|_2. \quad (7)$$

GNAT solves this nonlinear least-squares problem by the Gauss–Newton method, which is globally convergent under certain assumptions. This method delivers a solution that is *discrete optimal at each time step*: the solution minimizes the discrete residual associated with the tier I model over the trial subspace. This residual-minimization approach is mathematically equivalent to performing a Petrov–Galerkin projection with a test basis corresponding to $\frac{\partial R}{\partial w} \Phi_w$ (see Ref. [1]). Note that the fully discrete framework described in Section 3.2 enables discrete optimality to be achieved: the test basis depends on the discrete residual and thus depends on the time integrator, so it is not defined at the semi-discrete level.

Ref. [1] numerically demonstrated the superior accuracy delivered by the tier II Petrov–Galerkin ROM associated with Eq. (7) compared with its counterpart based on a (more commonly used) Galerkin projection when applied to a non-self-adjoint problem characterized by an unsymmetric residual Jacobian, which is typical in CFD. This strong performance is likely due to the discrete optimality property, which Galerkin projection lacks for such problems. However, for the relatively small class of CFD problems characterized by a symmetric residual Jacobian, a Galerkin projection is also discrete optimal, as it minimizes the discrete residual, albeit for a different norm [1].

3.3.2. Consistency

To ensure a consistent projection, the basis Φ_w can be computed by proper orthogonal decomposition (POD) using a specific set of snapshots collected from simulations performed using the tier I CFD model at the training inputs. Specifically, given a snapshot matrix $W \in \mathbb{R}^{N \times n_W}$, a POD basis $\Phi \in \mathbb{R}^{N \times n_\Phi}$ of dimension $n_\Phi \leq n_W$ is obtained by first computing the (thin) singular value decomposition (SVD)

$$W = U \Sigma V^T, \quad (8)$$

where the superscript T designates the transpose, the left-singular-vector matrix $U \equiv [u^1 \dots u^{n_W}] \in \mathbb{R}^{N \times n_W}$ satisfies $U^T U = I$, the singular-value matrix $\Sigma = \text{diag}(\sigma_i)$ satisfies $\sigma_1 \geq \sigma_2 \geq \dots \geq \sigma_{n_W} \geq 0$, and the right-singular-vector matrix $V \in \mathbb{R}^{n_W \times n_W}$ satisfies $V^T V = I$. Then, the sought-after POD basis is obtained by selecting the first $n_\Phi \leq n_W$ left singular vectors: $\Phi = [u^1 \dots u^{n_\Phi}]$. As a result, Φ has orthonormal columns and satisfies $\Phi^T \Phi = I$. Often, n_Φ is determined from an energy criterion such that the POD basis captures a fraction of the statistical energy of the snapshots.

Ref. [1] proved that the Petrov–Galerkin projection defined by Eq. (7) is consistent when Φ_w is computed by POD with snapshots of the form $\{w^n(\mu) - w^{n(0)}(\mu) \mid n = 1, \dots, n_t, \mu \in \mathcal{D}_{\text{train}}\}$, where $w^{n(0)} = w^{n-1}$, $n = 1, \dots, n_t$ denotes the initial guess for the Newton solver. This implies that the snapshots used for POD should correspond to the solution *increment* at each time step of the training simulations. This remark is noteworthy because most nonlinear model-reduction techniques reported in the literature employ a POD basis computed using snapshots $\{w^n(\mu) \mid n = 0, \dots, n_t, \mu \in \mathcal{D}_{\text{train}}\}$, which do not lead to a consistent projection.

Here, an alternative snapshot-collection procedure is proposed: $\{w^n(\mu) - w^0(\mu) \mid n = 1, \dots, n_t, \mu \in \mathcal{D}_{\text{train}}\}$. These snapshots also lead to a consistent projection under certain conditions. Appendix A discusses these conditions and contains the proof that both snapshot-collection procedures lead to a consistent Petrov–Galerkin projection.

3.4. Hyper-reduction

Solving the least-squares problem (7) by the Gauss–Newton method leads to the following iterations: for $k = 1, \dots, K$, solve the linear least-squares problem

$$s^{(k)} = \arg \min_{a \in \mathbb{R}^{n_w}} \|J^{(k)} \Phi_w a + R^{(k)}\|_2 \quad (9)$$

and set

$$w_r^{(k+1)} = w_r^{(k)} + \alpha^{(k)} s^{(k)}, \quad (10)$$

where K is determined by the satisfaction of a convergence criterion, $w_r^{(0)}$ is the initial guess (often taken to be the generalized coordinates computed at the previous time step), and $R^{(k)} \equiv R(w^0 + \Phi_w w_r^{(k)})$ and $J^{(k)} \equiv \frac{\partial R}{\partial w}(w^0 + \Phi_w w_r^{(k)})$ are the nonlinear residual and its Jacobian at iteration k , respectively. The step length $\alpha^{(k)}$ is computed by executing a line search in the direction $s^{(k)}$ to ensure convergence, or is set to the canonical step length of unity. Even though the dimension of the trial subspace is small, the computational cost of solving the above nonlinear least-squares problem scales with the dimension N of the tier I high-dimensional CFD model. As mentioned in the introduction, this is the computational bottleneck faced by many (if not all) projection-based nonlinear model reduction techniques. The role of hyper-reduction (referred to as system approximation in Ref. [1]) is to decrease this computational cost.

3.4.1. Optimality

To address the performance bottleneck identified above, GNAT employs the gappy POD data reconstruction technique [34]. In the context of GNAT, gappy POD leads to approximations of the one- and two-dimensional tensors $R^{(k)}$ and $J^{(k)} \Phi_w$, respectively, by computing only a small subset of their rows. Denoting by $\mathcal{I} \equiv \{i_1, i_2, \dots, i_{n_i}\} \subset \{1, \dots, N\}$ the set of n_i sample indices for which these functions are evaluated, the sample matrix is defined as

$$Z \equiv \mathbf{Z}(\mathcal{I}) \in \mathbb{R}^{N \times n_i}, \quad (11)$$

where

$$\begin{aligned} \mathbf{Z}(\mathcal{Y}) &\equiv \begin{bmatrix} e_{y_1} & \dots & e_{y_{n_y}} \end{bmatrix}^T \\ \mathcal{Y} &\equiv \{y_1, \dots, y_{n_y}\}, \end{aligned} \quad (12)$$

and e_i is the i th canonical unit vector.

Given these sample indices and bases $\Phi_R \in \mathbb{R}^{N \times n_R}$ and $\Phi_J \in \mathbb{R}^{N \times n_J}$, GNAT approximates $R^{(k)}$ and $J^{(k)}\Phi_w$ via gappy POD as follows:

$$\tilde{R}^{(k)} = \Phi_R [Z\Phi_R]^+ ZR^{(k)} \quad (13)$$

$$\widetilde{J^{(k)}\Phi_w} = \Phi_J [Z\Phi_J]^+ ZJ^{(k)}\Phi_w, \quad (14)$$

where the superscript $+$ designates the Moore–Penrose pseudo-inverse. Approximations (13)–(14) are discrete optimal in the sense that the error measures $\|ZR^{(k)} - Z\tilde{R}^{(k)}\|_2$ and $\|ZJ^{(k)}\Phi_w - Z\widetilde{J^{(k)}\Phi_w}\|_F$ monotonically decrease as columns are added to Φ_R and Φ_J , respectively.

Substituting $R^{(k)} = \tilde{R}^{(k)}$ and $J^{(k)}\Phi_w = \widetilde{J^{(k)}\Phi_w}$ in Eqs. (9)–(10) and assuming that $\Phi_J^T \Phi_J = I_{n_J}$ — which is easily achievable by computing Φ_J using POD — the tier II Petrov–Galerkin iterations are transformed into the tier III GNAT iterations

$$s^{(k)} = \arg \min_{v \in \mathbb{R}^{n_w}} \|AZJ^{(k)}\Phi_w v + BZR^{(k)}\|_2 \quad (15)$$

$$w_r^{(k+1)} = w_r^{(k)} + \alpha^{(k)} s^{(k)}. \quad (16)$$

Here, the matrices $A = [Z\Phi_J]^+ \in \mathbb{R}^{n_J \times n_i}$ and $B = \Phi_J^T \Phi_R [Z\Phi_R]^+ \in \mathbb{R}^{n_J \times n_i}$ can be computed *a priori*, during the offline stage.

Note that in CFD, the Jacobian matrix is usually sparse. Hence, computing $ZR^{(k)}$ and $ZJ^{(k)}\Phi_w$ does not require access to all entries of the fluid state vector. For this reason, let \mathcal{J} denote the minimum-cardinality set of indices of the fluid state vector that influences the residual entries corresponding to sample-index set \mathcal{I} . GNAT requires access to only the ‘masked’ state $\bar{Z}^T \bar{Z}w$, where $\bar{Z} \equiv \mathbf{Z}(\mathcal{J})$ and $n_j \equiv |\mathcal{J}|$. The algebraic products implied by this masked state vector can be obtained by evaluating only the \mathcal{J} entries of the state w .

After the index sets \mathcal{I} and \mathcal{J} are determined (see Section 5.2 for a discussion on determining these index sets), the online GNAT iterations executed at each time step can proceed as follows:

1. Compute $\bar{Z}\tilde{w}^{(k)} = \bar{Z}w^0 + \bar{Z}\Phi_w w_r^{(k)}$, which requires updating only n_j entries of the state.
2. Compute $C^{(k)} = Z \frac{\partial R}{\partial w} \left(\bar{Z}^T \bar{Z}\tilde{w}^{(k)} \right) \bar{Z}^T \bar{Z}\Phi_w$ and $D^{(k)} = ZR(\bar{Z}^T \bar{Z}\tilde{w}^{(k)})$, which necessitates computing only n_i rows of $R^{(k)}$ and $J^{(k)}\Phi_w$, respectively.
3. Compute the low-dimensional products $AC^{(k)}$ and $BD^{(k)}$.
4. Solve the reduced-order least-squares problem $s^{(k)} = \arg \min_{v \in \mathbb{R}^{n_w}} \|AC^{(k)}v + BD^{(k)}\|_2$.
5. Update the n_w generalized coordinates $w_r^{(k+1)}$ using Eq. (16).

Because none of the above computations scales with the large dimension N of the high-dimensional CFD model, the cost of the online stage of GNAT is typically very small.

3.4.2. Consistency

To ensure consistency in the hyper-reduction procedure outlined above, the bases Φ_R and Φ_J can be constructed using POD with snapshots that verify certain properties. For example, Ref. [1] introduced three conditions on the snapshots that together ensure consistency. These conditions lead to a hierarchy of snapshot-collection procedures that trade consistency for more affordable offline resources such as core-hours and storage. Table 1 summarizes these procedures.

Procedure 3 ensures a consistent hyper-reduction because it satisfies all three conditions that together are sufficient for consistency. However, it is infeasible for most problems as it requires storing either $n_w + 1$ vectors or the (sparse) high-dimensional residual Jacobian at each Newton step of the training simulations.

Procedure identifier	0	1	2	3
Snapshots for $R^{(k)}$	$R_I^{(k)}$	$R_{II}^{(k)}$	$R_{II}^{(k)}$	$R_{II}^{(k)}$
Snapshots for $J^{(k)}\Phi_w$	$R_I^{(k)}$	$R_{II}^{(k)}$	$[J^{(k)}\Phi_w s^{(k)}]_{II}$	$[J^{(k)}\Phi_w]_{II}$
# of simulations per training input	1	2	2	2
# of snapshots per Newton iteration	1	1	2	$n_w + 1$
# of conditions for consistency satisfied	0	1	2	3

Table 1 Snapshot-collection procedures for the tier III GNAT ROM. The indicated snapshots are saved at each Newton iteration for the training simulations. Subscripts I and II specify the tier of the model for which the snapshots are collected.

Procedure 2 does not provide a consistent hyper-reduction, although it satisfies two of the three consistency conditions. Furthermore, it is computationally feasible as it requires saving only two vectors per Newton step.

Procedure 1 is more economical than procedure 2, as it requires saving only one vector per Newton iteration and it computes one fewer POD basis. Further, procedure 1 uses the same POD basis for the residual and its Jacobian; when this occurs, the GNAT iterations are equivalent to the Gauss–Newton iterations for minimizing $\tilde{R}^{(k)}$, which can abet convergence (see Appendix B). However, procedure 1 satisfies only one of the three consistency conditions.

Procedure 0 requires performing only one tier I simulation for each training input and therefore is similar to conventional approaches for collecting snapshots [22, 23, 24, 31, 32]; however, it satisfies none of the aforementioned consistency conditions. Appendix B offers an additional discussion of these snapshot-collection procedures.

3.5. Computation of outputs

After GNAT computes generalized coordinates w_r^n , $n = 1, \dots, n_t$ for online inputs $\check{\mu} \in \mathcal{D}$, the outputs z can be computed. Because the objective is to ensure that no online computation scales with the large dimension N of the high-dimensional CFD model, an alternative method to computing the outputs via Eq. (17) below is needed:

$$z = G(w^0, w^0 + \Phi_w w_r^1, \dots, w^0 + \Phi_w w_r^{n_t}, \check{\mu}). \quad (17)$$

Indeed, this expression implies matrix–vector products of the form $\Phi_w y$ that entail $\mathcal{O}(Nn_w)$ operations.

In general, the outputs cannot be computed during the online stage of a GNAT simulation, because the outputs may depend on entries of the state vector that are not included in \mathcal{J} . For example, the drag force exerted on an immersed body depends on the conserved fluid variables at all nodes located on its wet surface, but the index set \mathcal{J} will not generally include all of these indices.

Instead, the outputs can be efficiently computed in a post-processing step that accesses only the computed generalized coordinates w_r^n for $n = 1, \dots, n_t$, and the rows of the initial condition w^0 and POD basis Φ_w needed for the desired output computation. To this effect, let \mathcal{K} denote the minimum-cardinality set of indices of the fluid state vector that affects the output computation. Given generalized coordinates computed by GNAT online, the outputs can be computed as

$$z = G(\underline{Z}^T \underline{Z} w^0, \underline{Z}^T \underline{Z} w^0 + \underline{Z}^T \underline{Z} \Phi_w w_r^1, \dots, \underline{Z}^T \underline{Z} w^0 + \underline{Z}^T \underline{Z} \Phi_w w_r^{n_t}, \check{\mu}), \quad (18)$$

where $\underline{Z} \equiv \mathbf{Z}(\mathcal{K})$ and $n_k \equiv |\mathcal{K}|$. This approach entails products of the form $\underline{Z}^T \underline{Z} \Phi_w y$ that require performing computations with only the \mathcal{K} rows of Φ_w and incur $\mathcal{O}(n_k n_w)$ operations. This operation count is small if $n_k \ll N$. Fortunately, this condition holds in the case of spatially local outputs such as the value of flow variables at several points in the domain, or the lift and drag, which are associated with the wet surface of a body. This condition does not hold for spatially global outputs.

3.6. Offline-online decomposition

In summary, GNAT builds a ‘global’ ROM — that is, a ROM trained at multiple points in the input-parameter space — and performs a ROM simulation in two stages as follows:

Offline stage

1. Perform tier I simulations at various training inputs $\mathcal{D}_{\text{train}}$. Collect snapshots of the fluid state vector (and snapshots of the residual if using snapshot-collection procedure 0 of Table 1). during these training simulations.
2. Compute POD basis Φ_w using the collected fluid-state snapshots.
3. If snapshot-collection procedure 1, 2, or 3 is employed, perform tier II simulations at training inputs $\mathcal{D}_{\text{train}}$. Collect snapshots for the residual and its Jacobian during these training simulations as specified by Table 1 .
4. Compute POD bases Φ_R and Φ_J using the collected snapshots. To ensure the matrix $AZJ^{(k)}\Phi_w$ has full rank, enforce $n_J \geq n_w$.
5. Determine the sample-index set \mathcal{I} (for example, see Section 5.2), and consequently index set \mathcal{J} . To ensure uniqueness for the gappy POD approximations, enforce $n_i \geq n_R$ and $n_i \geq n_J$.
6. Compute matrices $A = [Z\Phi_J]^+$ and $B = \Phi_J^T \Phi_R [Z\Phi_R]^+$ to be used during online computations.
7. Determine the index set \mathcal{K} related to output computation.
8. Using index sets \mathcal{I} , \mathcal{J} , and \mathcal{K} , construct the associated sample meshes (see Section 5) — which are tiny subsets of the CFD mesh — on which to perform the online stage of a GNAT simulation as summarized below.

Online stage

1. Apply Algorithm 1 to perform the GNAT ROM simulation for inputs $\check{\mu} \in \mathcal{D}$ specified online.
2. Apply Algorithm 2 to compute the desired outputs.

4. Error bounds

Here, error bounds are developed for any discrete nonlinear model-reduction method assuming that time discretization is performed using the backward-Euler scheme. These bounds highlight the advantages of the GNAT method, as it minimizes components of these error bounds.

When Eq. (1) is time discretized using the backward-Euler scheme, the residual corresponding to time step n , input parameters μ , and the sequence of states computed by the high-dimensional CFD model w^n , $n = 0, \dots, n_t$ can be written as

$$R^n(w^{n+1}; \mu) = w^{n+1} - w^n - \Delta t F(w^{n+1}, t^{n+1}; \mu). \quad (19)$$

Proposition 4.1. *Assume $f : (w, t; \mu) \mapsto w - \Delta t F(w, t; \mu)$ satisfies the following inverse Lipschitz continuity condition for the online input $\check{\mu} \in \mathcal{D}$*

$$\frac{\|f(w, t^n; \check{\mu}) - f(y, t^n; \check{\mu})\|}{\|w - y\|} \geq \varepsilon > 0, \quad \forall n \in \{1, \dots, n_t\}. \quad (20)$$

Furthermore, assume that the high-dimensional CFD model employs the backward-Euler scheme for time-integration and computes states w^n , $n = 1, \dots, n_t$ that satisfy an absolute tolerance for the residual

$$\|R^n(w^{n+1}; \check{\mu})\| \leq \epsilon_{\text{Newton}}, \quad \forall n \in \{0, \dots, n_t - 1\}. \quad (21)$$

Algorithm 1 Online step 1: GNAT ROM simulation

Input: online matrices A and B , online inputs $\check{\mu} \in \mathcal{D}$, initial condition $\bar{Z}w^0(\check{\mu})$, and state POD basis $\bar{Z}\Phi_w$

Output: generalized coordinates $w_r^n(\check{\mu})$, $n = 1, \dots, n_t$

- 1: **for** $n = 0, \dots, n_t - 1$ **do**
- 2: Choose initial guess $w_r^{n+1(0)}$ (e.g., $w_r^{n+1(0)} \leftarrow w_r^n$ with $w_r^0 = 0$).
- 3: $k \leftarrow 0$
- 4: **while** not converged **do**
- 5: Compute

$$C^{n(k)} = Z \frac{\partial R^n}{\partial w} \left(\bar{Z}^T \bar{Z} w^0 + \bar{Z}^T \bar{Z} \Phi_w w_r^{n+1(k)}; \check{\mu} \right) \bar{Z}^T \bar{Z} \Phi_w$$

$$D^{n(k)} = Z R^n \left(\bar{Z}^T \bar{Z} w^0 + \bar{Z}^T \bar{Z} \Phi_w w_r^{n+1(k)}; \check{\mu} \right).$$

- 6: Compute

$$s^{n+1(k)} = \arg \min_{v \in \mathbb{R}^{n_w}} \|AC^{n(k)}v + BD^{n(k)}\|_2$$

$$w_r^{n+1(k+1)} = w_r^{n+1(k)} + \alpha^{n+1(k)} s^{n+1(k)},$$

where $\alpha^{n+1(k)}$ is computed via line search or is set to 1.

- 7: $\bar{Z}\tilde{w}^{n+1(k+1)} \leftarrow \bar{Z}w^0 + \bar{Z}\Phi_w w_r^{n+1(k+1)}$
 - 8: $k \leftarrow k + 1$
 - 9: **end while**
 - 10: Set $w_r^{n+1}(\check{\mu}) \leftarrow w_r^{n+1(k)}$ and save it; it will be used to compute outputs using Algorithm 2.
 - 11: **end for**
-

Algorithm 2 Online step 2: computation of outputs

Input: online inputs $\check{\mu} \in \mathcal{D}$, generalized coordinates $w_r^n(\check{\mu})$, $n = 1, \dots, n_t$, initial condition $\underline{Z}w^0(\check{\mu})$, and state POD basis $\underline{Z}\Phi_w$

Output: outputs z

- for** $n = 1, \dots, n_t$ **do**
 - $\underline{Z}\tilde{w}^n \leftarrow \underline{Z}w^0 + \underline{Z}\Phi_w w_r^n$
 - end for**
 - Compute $z = G(\underline{Z}^T \underline{Z} w^0, \dots, \underline{Z}^T \underline{Z} \tilde{w}^{n_t}, \check{\mu})$
-

Then, for any sequence of states \tilde{w}^n , $n = 0, \dots, n_t$ satisfying $\tilde{w}^0 = w^0$, a global error bound for the approximation of the state at the n -th time step is given by

$$\|w^n - \tilde{w}^n\| \leq \sum_{k=1}^n a^k b_{n-k} \leq \sum_{k=1}^n a^k c_{n-k} \leq \sum_{k=1}^n a^k d_{n-k}, \quad (22)$$

where

$$\begin{aligned}
a &\equiv \sup_{n \in \{1, \dots, n_t\}} \sup_{w \neq y} \frac{\|w - y\|}{\|f(w, t^n; \check{\mu}) - f(y, t^n; \check{\mu})\|} \\
b_n &\equiv \epsilon_{\text{Newton}} + \|\tilde{R}^n(\tilde{w}^{n+1}; \check{\mu})\| \\
c_n &\equiv \epsilon_{\text{Newton}} + \|P\tilde{R}^n(\tilde{w}^{n+1}; \check{\mu})\| + \|(I - P)\tilde{R}^n(\tilde{w}^{n+1}; \check{\mu})\| \\
d_n &\equiv \epsilon_{\text{Newton}} + \|P\tilde{R}^n(\tilde{w}^{n+1}; \check{\mu})\| + \|\mathbf{R}^{-1}\| \|(I - \mathbb{P})\tilde{R}^n(\tilde{w}^{n+1}; \check{\mu})\| \\
P &\equiv \Phi_R [Z\Phi_R]^+ Z \\
\mathbb{P} &\equiv \Phi_R \Phi_R^T \\
Z\Phi_R &\equiv \mathbf{Q}\mathbf{R},
\end{aligned} \tag{23}$$

where $\mathbf{Q} \in \mathbb{R}^{n_i \times n_R}$, $\mathbf{R} \in \mathbb{R}^{n_R \times n_R}$, and $\tilde{R}^n(w; \mu) = w - \tilde{w}^n - \Delta t F(w, t^n; \mu)$.

Appendix C provides a proof of the above error bounds. Their consequences include:

- Justification for the minimum-residual approach taken by the tier II Petrov–Galerkin ROM. Namely, by computing $\tilde{w}^{n+1} = \arg \min_{\tilde{w} \in w^{n+1(0)} + \mathcal{Y}} \|\tilde{R}^n(\tilde{w}; \check{\mu})\|$, the tier II Petrov–Galerkin ROM selects the element of the trial subspace that minimizes b_n , $n = 1, \dots, n_t$. This in turn minimizes the tightest error bound in (22).
- Justification for using $\Phi_R = \Phi_J$ in GNAT (snapshot-collection procedures 0 and 1). In this case, the GNAT iterations are equivalent to applying the Gauss–Newton method for minimizing $\|P\tilde{R}^n(\tilde{w}^{n+1}; \check{\mu})\|$. As a result, GNAT computes $\tilde{w}^{n+1} = \arg \min_{\tilde{w} \in w^{n+1(0)} + \mathcal{Y}} \|P\tilde{R}^n(\tilde{w}; \check{\mu})\|$, which is the element of the trial subspace that minimizes the second term of both c_n and d_n , $n = 1, \dots, n_t$.
- Justification for computing Φ_R via POD. When computed by POD, the basis Φ_R is the orthogonal basis of dimension n_R that minimizes the average projection error over the set of residual snapshots; this projection error appears as the last term of d_n .
- The tightest bound in (22) is computable by the tier II Petrov–Galerkin ROM if the Lipschitz constant a can be computed or estimated. This is due to the computability of b_n : it requires only the tolerance ϵ_{Newton} and the residual norm at each time step.
- The bound $\sum_{k=1}^n a^k c_{n-k}$ (resp. $\sum_{k=1}^n a^k d_{n-k}$) is computable by GNAT if the Lipschitz constant a can be computed or estimated and the projection error $\|(I - P)\tilde{R}^n(\tilde{w}^{n+1}; \check{\mu})\|$ (resp. $\|(I - \mathbb{P})\tilde{R}^n(\tilde{w}^{n+1}; \check{\mu})\|$) can be computed or estimated. This is due to the computability of $\|P\tilde{R}^n(\tilde{w}^{n+1}; \check{\mu})\| = \|[Z\Phi_R]^+ Z\tilde{R}^n(\tilde{w}^{n+1}; \check{\mu})\|$. The projection error $\|(I - P)\tilde{R}^n(\tilde{w}^{n+1}; \check{\mu})\|$ can be estimated by

$$\begin{aligned}
\|(I - P)\tilde{R}^n(\tilde{w}^{n+1}; \check{\mu})\| &\approx \|(\Phi'_R [Z\Phi'_R]^+ - \Phi_R [Z\Phi_R]^+) Z\tilde{R}^n(\tilde{w}^{n+1}; \check{\mu})\| \\
&= \left\| \left([Z\Phi'_R]^+ - \begin{bmatrix} [Z\Phi_R]^+ \\ 0_{(n'_R - n_R) \times n_i} \end{bmatrix} \right) Z\tilde{R}^n(\tilde{w}^{n+1}; \check{\mu}) \right\|,
\end{aligned} \tag{24}$$

where $\Phi'_R \equiv [\phi_1^{n'_R} \cdots \phi_{n'_R}^{n'_R}]$ for some $n'_R > n_R$ (following Ref. [33]). Alternatively, the projection error $\|(I - \mathbb{P})\tilde{R}^n(\tilde{w}^{n+1}; \check{\mu})\|$ can be approximated by the sum of the squares of the singular values neglected by Φ_R (following Ref. [35]).

5. Implementation of online computations and post-processing

5.1. Sample mesh concept

A quick inspection of Algorithm 1 reveals that the online stage of the GNAT method performs CFD computations in only Step 5 of this algorithm. Furthermore, these computations require, manipulate, and generate information only at the nodes of the CFD mesh associated with the index sets \mathcal{I} and \mathcal{J} described in Section 3.4.1. Similarly, an inspection of Algorithm 2 for output computation reveals that this algorithm requires online access only to information pertaining to the nodes of the CFD mesh associated with the index set \mathcal{K} described in Section 3.5. From these two observations, it follows that both online algorithms can be effectively implemented by constructing in each case a ‘sample mesh’ tailored to the computations to be performed. This concept is related to the subgrid idea recently proposed in [25, 36], but differs from it primarily in the node sampling algorithm as discussed in Section 5.2.

For the purpose of building and exploiting the GNAT ROM, the sample mesh used to execute Algorithm 1 must contain only the nodes associated with index sets \mathcal{I} and \mathcal{J} , and the geometrical entities (e.g., edges, faces, cells) associated with these nodes. For example, consider the case where the flow solver of interest operates on unstructured tetrahedral meshes and is based on a second-order finite-volume spatial discretization, where the discrete unknowns are located at the mesh nodes and the fluxes are computed across the boundaries of control volumes. Here, the control volumes (or dual cells) are constructed by connecting the centroids of the triangular faces and the midpoints of the edges. The union of these control volumes is often referred to as the dual CFD mesh. In this case, the sample mesh is constructed by assembling the nodes associated with the index sets \mathcal{I} and \mathcal{J} , and the edges, faces, and cells required to allow the same CFD solver to perform the computations in Step 5 of Algorithm 1 as if it were operating on the original CFD mesh. Figure 2 illustrates this case in two dimensions. Note that although the sample mesh shown in this figure is simply connected, this property is not required. The reason for this is that the sample mesh has no specific geometrical meaning and therefore no connectivity requirement aside from that imposed by the stencil of the flow solver’s spatial discretization scheme.

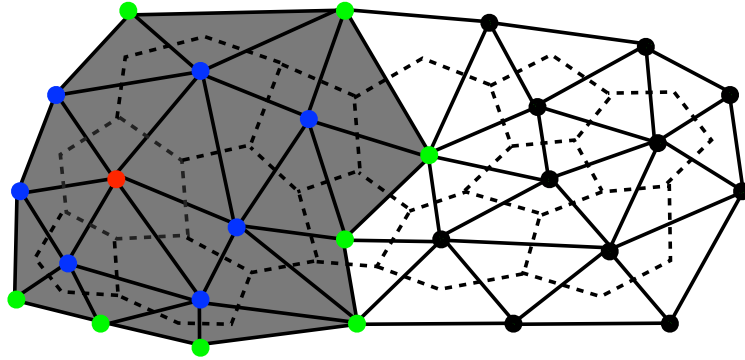


Figure 2 Original and sample CFD meshes for online GNAT computations based on a second-order finite volume method operating on a dual mesh. The original mesh is defined by all triangles, control volumes (dashed lines), edges, and nodes. The sample mesh is defined by the gray-shaded triangles, associated edges, all control volumes fully contained within the gray region, and the red, blue, and green nodes. The residual and its Jacobian are computed at the red node (which defines \mathcal{I}), and the fluid state vector is computed at the red, blue, and green nodes (which together define \mathcal{J}).

The second sample mesh used to execute Algorithm 2 for output computation must contain only the nodes associated with the index set \mathcal{K} , and their corresponding geometrical entities. For example, when the desired outputs are the lift and drag, the sample mesh is the wet surface mesh — that is, the collection of faces and nodes lying on the obstacle around which the flow is computed — and any other geometrical entity the flow solver requires to compute the outputs.

As previously mentioned, one major advantage of the sample-mesh approach is that it allows the same flow solver that was used for offline, high-dimensional CFD computations to be used for online, low-dimensional computations. Consequently, the online ROM computations can be automatically distributed and parallelized in the same manner as their large-scale CFD counterparts. The ROM’s performance can also be expected to scale (in the weak sense, or the scaled speedup metric) in a similar manner to that of the large-scale flow computations using the same CFD solver. However, because its size is typically a *tiny fraction* of that of the original CFD mesh, the sample mesh can be expected to require significantly fewer computational cores and lead to simulations requiring far fewer core-hours than its large-scale counterpart; Section 6.2 demonstrates this.

Determining the index set \mathcal{K} is a trivial task. For this reason, constructing the sample mesh for output computation is also straightforward. However, determining the sample-index set \mathcal{I} at which to compute the residual and its Jacobian is a more delicate matter that is discussed next.

5.2. Underlying node sampling algorithm

Several algorithms have been proposed in the literature for selecting the sample indices that define the sample matrix Z . Usually, these algorithms are tailored to the hyper-reduction procedure they are designed to support. For example, for the various forms of empirical interpolation outlined in Section 1, several algorithms for selecting sample indices have been developed around the objective of minimizing the error in the interpolated snapshots [22, 31, 25], the difference between the interpolated snapshots and their orthogonal projections onto the subspace of approximation [37, 32], and the condition number of the normal-equations matrix used for interpolation or least-squares approximation [38, 29]. However, because these algorithms are sensitive to differences in scale between different conservation equations, they are not particularly suitable for CFD applications, as they would lead to a biased treatment of the multiple conservation equations defined at each mesh node. For this reason, Ref. [39] applied the greedy sampling algorithm adopted in Refs. [22, 31, 25] to each conservation equation separately. However, this approach causes the conservation equations to be sampled at different sets of nodes. This not only complicates the implementation of online CFD computations, it also leads to a larger subgrid than necessary and therefore to computationally suboptimal nonlinear ROM simulations.

Here, Algorithm 3 is proposed for determining the sample nodes from a given CFD mesh, and therefore constructing the sample-index set \mathcal{I} and sample matrix Z . This algorithm is based on the greedy method presented in Refs. [22, 31, 25]. This choice is made because this method attempts to minimize the error $\|(I - P)\tilde{R}^n(\tilde{w}^{n+1}; \tilde{\mu})\|$ associated with the gappy POD projection of the residual, and therefore the third term of the coefficient c_n (23) characterizing the error bound (22). However, Algorithm 3 distinguishes itself from the method described in Refs. [22, 31, 25] in a few noteworthy aspects. First, it allows for overdetermined least-squares matrices as opposed to relying on interpolation of the nonlinear function. Secondly, it allows different bases to be used to approximate the residual and its Jacobian. Finally, it operates directly on the mesh nodes instead of the algebraic indices. Thus, the sample-index set \mathcal{I} consists of the degrees of freedom associated with the nodes in set $\mathcal{N} \equiv \{\mathbf{n}_1, \mathbf{n}_2, \dots, \mathbf{n}_{n_s}\}$. Because of this latter minor albeit distinctive feature, Algorithm 3 treats all conservation equations in a balanced manner, does not lead to a larger-than-necessary sample mesh, and therefore does not introduce from the outset a computational inefficiency in the online ROM computations.

Remark 2 The sample-node set \mathcal{N} can be seeded with nodes of the CFD mesh that are deemed important due to their strategic locations. In particular, it is essential that at least one sample node lies on the inlet or outlet boundary of the problem, if such a boundary exists. It is equally essential that each input variable μ_i , $i = 1, \dots, d$ affects the value of the residual at at least one sample node. If the above conditions are not met, the hyper-reduced GNAT model will be blind to the boundary conditions and inputs [40].

6. Applications

To illustrate the ability of GNAT to reduce the dimension and complexity of highly nonlinear CFD models while maintaining a high level of accuracy, this section considers two examples. The first one is an academic

Algorithm 3 Greedy algorithm for selecting sample nodes from a given CFD mesh

Input: Φ_R ; Φ_J ; target number of sample nodes n_s ; seeded sample-node set \mathcal{N} (see **Remark 2**); number of working columns of Φ_R and Φ_J denoted by $n_c \leq \min(n_R, n_J, \nu n_s)$, where ν denotes the number of unknowns at a node (for example, $\nu = 5$ for three-dimensional compressible flows without a turbulence model).

Output: sample-node set \mathcal{N}

```

1: Compute the additional number of nodes to sample:  $n_a = n_s - |\mathcal{N}|$ 
2: Initialize counter for the number of working basis vectors used:  $n_b \leftarrow 0$ 
3: Set the number of greedy iterations to perform:  $n_{it} = \min(n_c, n_a)$ 
4: Compute the maximum number of right-hand sides in the least-squares problems:  $n_{RHS} = \text{ceil}(n_c/n_a)$ 
5: Compute the minimum number of working basis vectors per iteration:  $n_{ci, \min} = \text{floor}(n_c/n_{it})$ 
6: Compute the minimum number of sample nodes to add per iteration:  $n_{ai, \min} = \text{floor}(n_a n_{RHS}/n_c)$ 
7: for  $i = 1, \dots, n_{it}$  do {greedy iteration loop}
8:   Compute the number of working basis vectors for this iteration:  $n_{ci} \leftarrow n_{ci, \min}$ ;
   if  $(i \leq n_c \bmod n_{it})$ , then  $n_{ci} \leftarrow n_{ci} + 1$ 
9:   Compute the number of sample nodes to add during this iteration:  $n_{ai} \leftarrow n_{ai, \min}$ ;
   if  $(n_{RHS} = 1)$  and  $(i \leq n_a \bmod n_c)$ , then  $n_{ai} \leftarrow n_{ai} + 1$ 
10:  if  $i = 1$  then
11:     $\begin{bmatrix} \mathbf{R}^1 & \dots & \mathbf{R}^{n_{ci}} \end{bmatrix} \leftarrow \begin{bmatrix} \phi_R^1 & \dots & \phi_R^{n_{ci}} \end{bmatrix}$ 
12:     $\begin{bmatrix} \mathbf{J}^1 & \dots & \mathbf{J}^{n_{ci}} \end{bmatrix} \leftarrow \begin{bmatrix} \phi_J^1 & \dots & \phi_J^{n_{ci}} \end{bmatrix}$ 
13:  else
14:    for  $q = 1, \dots, n_{ci}$  do {basis vector loop}
15:       $\mathbf{R}^q \leftarrow \phi_R^{n_b+q} - \begin{bmatrix} \phi_R^1 & \dots & \phi_R^{n_b} \end{bmatrix} \alpha$ , with  $\alpha = \arg \min_{\gamma \in \mathbb{R}^{n_b}} \left\| \begin{bmatrix} Z\phi_R^1 & \dots & Z\phi_R^{n_b} \end{bmatrix} \gamma - Z\phi_R^{n_b+q} \right\|_2$ 
16:       $\mathbf{J}^q \leftarrow \phi_J^{n_b+q} - \begin{bmatrix} \phi_J^1 & \dots & \phi_J^{n_b} \end{bmatrix} \beta$ , with  $\beta = \arg \min_{\gamma \in \mathbb{R}^{n_b}} \left\| \begin{bmatrix} Z\phi_J^1 & \dots & Z\phi_J^{n_b} \end{bmatrix} \gamma - Z\phi_J^{n_b+q} \right\|_2$ 
17:    end for
18:  end if
19:  for  $j = 1, \dots, n_{ai}$  do {sample node loop}
20:    Choose node with largest average error:  $n \leftarrow \arg \max_{l \notin \mathcal{N}} \sum_{q=1}^{n_{ci}} \left( \sum_{i \in \delta(l)} ((\mathbf{R}_i^q)^2 + (\mathbf{J}_i^q)^2) \right)$ ,
    where  $\delta(l)$  denotes the degrees of freedom associated with node  $l$ .
21:     $\mathcal{N} \leftarrow \mathcal{N} \cup \{n\}$ 
22:  end for
23:   $n_b \leftarrow n_b + n_{ci}$ 
24: end for

```

Table 2 Offline and online inputs for the IBVP (25)–(27)

Input variables	Training input #1 μ^1	Training input #2 μ^2	Training input #3 μ^3	Online input $\check{\mu}$
a	3	6	9	4.5
b	0.02	0.05	0.075	0.038

problem based on Burgers’ equation. It features a moving shock, and therefore highlights GNAT’s potential for unsteady CFD problems with moving discontinuities. In this one-dimensional example, GNAT is applied in a prediction scenario — that is, for the (most relevant) case where the values of the input variables change between the offline training simulations and the online simulation. The second example pertains to the computation of the Ahmed body wake flow [41], which is a well-known CFD benchmark problem in the automotive industry. The CFD model employed for this three-dimensional problem is characterized by millions of unknowns and therefore incurs time-consuming offline computations. For this reason, GNAT is applied in this example in reproduction mode only — that is, for the (preliminary) scenario where the online input-variable values are identical to their training counterparts. Nevertheless, this example demonstrates GNAT’s performance on a realistic, large-scale turbulent flow problem, and contrasts it with that of other nonlinear model-reduction methods.

6.1. Parameterized inviscid Burgers’ equation

This numerical experiment employs the problem setup described in Ref. [27]. Consider the parameterized initial boundary value problem (IBVP)

$$\frac{\partial U(x,t)}{\partial t} + \frac{1}{2} \frac{\partial (U^2(x,t))}{\partial x} = 0.02e^{bx} \quad (25)$$

$$U(0,t) = a, \quad \forall t > 0 \quad (26)$$

$$U(x,0) = 1, \quad \forall x \in [0, 100], \quad (27)$$

where a and b are two real-valued input variables. This problem is discretized using Godunov’s scheme, which leads to a finite-volume formulation. The one-dimensional domain is discretized using a grid with 4001 nodes corresponding to coordinates $x_i = i \times (100/4000)$, $i = 0, \dots, 4000$. Hence, the resulting CFD model is of dimension $N = 4000$. The solution $U(x,t)$ is computed in the time interval $t \in [0, 4000]$ using a uniform computational time-step size $\Delta t = 0.05$, leading to $n_t = 1000$ total time steps. Because there is only one unknown per node, each sample node corresponds to a single sample index.

First, a GNAT model is constructed using snapshot-collection procedure 2 (see Table 1) and the following parameters: $n_w = 50$, $n_R = 160$, $n_J = 70$ and $n_i = 160$. It is trained for the solution of the IBVP (25)–(27) using the values of the boundary-condition parameter a and source-term parameter b reported in columns 2–4 of Table 2.

Next, the resulting global GNAT ROM is applied online to the solution of the IBVP (25)–(27) configured with the new values of a and b shown in column 5 of Table 2. A reference solution for this problem is also computed using the high-dimensional CFD model. Both solutions are graphically depicted in Figure 3 and were computed using a single processor.

The reader can observe that the GNAT prediction closely matches the reference solution in general. Although oscillations in the GNAT solution are apparent at $t = 2.5$, they dissipate over time. The relative time-averaged discrepancy between the GNAT solution and the reference high-dimensional CFD solution as measured in the Euclidean norm of the state vector is only 1.26%. The high-dimensional CFD solution took 1167 times longer to complete than the online GNAT solution; this showcases the improved CPU performance delivered by the GNAT ROM.

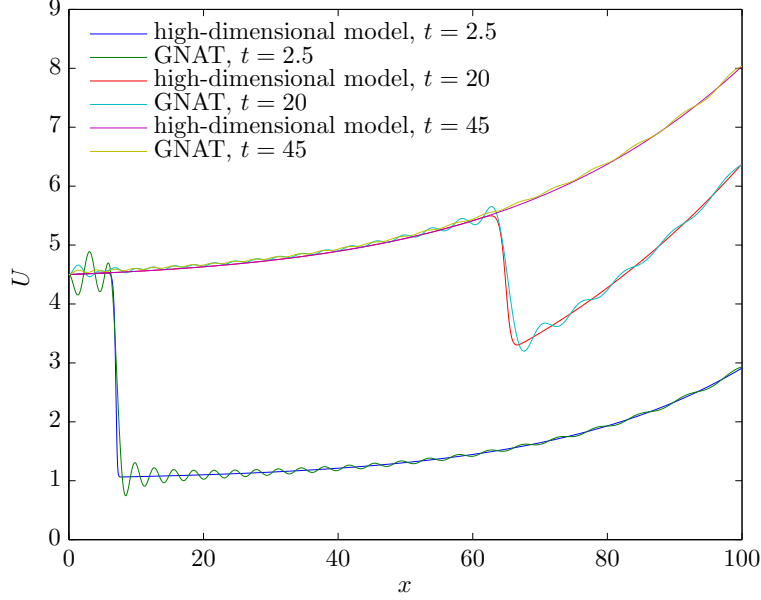


Figure 3 Performance of GNAT in predictive mode for the IBVP (25)–(27)

6.2. Ahmed-body wake flow

6.2.1. Preliminaries

To assess GNAT’s performance on large-scale CFD applications, GNAT is implemented in the massively parallel compressible-flow solver AERO-F [42, 43]. For turbulent, viscous flow computations, this finite-volume CFD code offers various RANS and LES turbulence models, as well as a wall function. It performs a second-order semi-discretization of the convective fluxes using a method based on the Roe, HLLE, or HLLC upwind scheme. It can also perform second- and fourth-order explicit and implicit temporal discretizations using a variety of time integrators. The GNAT implementation in AERO-F is characterized by the sample-mesh concept described in Section 5. All linear least-squares problems and singular value decompositions are computed in parallel using the ScaLAPACK library [44]. AERO-F is used here to demonstrate GNAT’s potential when applied to a realistic, large-scale, nonlinear benchmark CFD problem: turbulent flow around the Ahmed body.

The Ahmed-body geometry [41] is a simplified car geometry. It can be described as a modified parallelepiped featuring round corners at the front end and a slanted face at the rear end (see Figure 4). Depending on the inclination of this face, different flow characteristics and wake structure may be observed. For a slant angle $\varphi \geq 30^\circ$, the flow features a large detachment. For smaller slant angles, the flow reattaches on the slant. Consequently, the drag coefficient suddenly decreases when the slant angle is increased beyond its critical value of $\varphi = 30^\circ$. Due to this phenomenon, predicting the flow past the Ahmed body for varying slant angles has become a popular benchmark in the automotive industry.

This work considers the subcritical angle $\varphi = 20^\circ$ and treats the drag coefficient $C_D = \frac{D}{\frac{1}{2}\rho_\infty V_\infty^2}$ around the body as the output of interest. The free-stream velocity is set to $V_\infty = 60$ m/s, and the Reynolds number based on a reference length of 1.0 m is set to $\text{Re} = 4.29 \times 10^6$. The free-stream angle of attack is set to 0° .

6.2.2. High-dimensional CFD model

The high-dimensional CFD model corresponds to an unsteady Navier–Stokes simulation using AERO-F’s DES turbulence model and wall function. The fluid domain is discretized by a mesh with 2,890,434 nodes and 17,017,090 tetrahedra (Figure 5). A symmetry plane is employed to exploit the symmetry of the body about the x – z plane. Due to the turbulence model and three-dimensional domain, the number of conservation

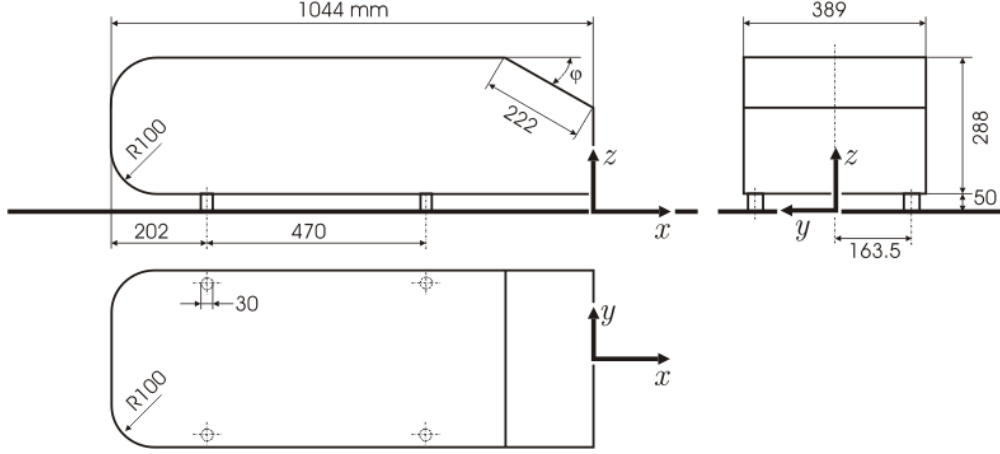


Figure 4 Geometry of the Ahmed body (from Ref. [45])

equations per node is $\nu = 6$, and therefore the dimension of the CFD model is $N = 17,342,604$. Roe's scheme is employed to discretize the convective fluxes; a linear variation of the solution is assumed within each control volume, which leads to a second-order space-accurate scheme.

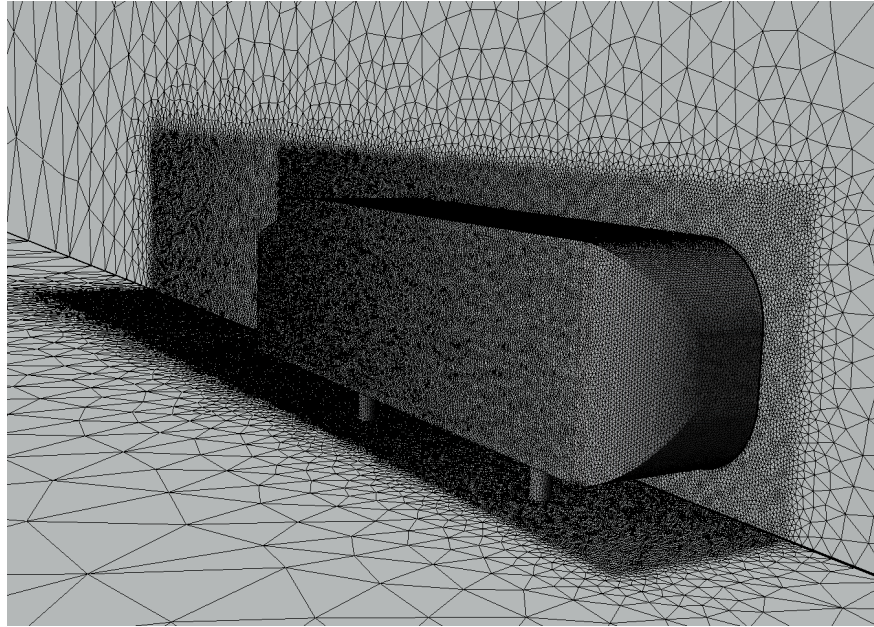


Figure 5 CFD mesh with 2,890,434 grid points and 17,017,090 tetrahedra (partial view, $\varphi = 20^\circ$). Darker areas indicate a more refined area of the mesh.

Flow simulations are performed within a time interval $t \in [0 \text{ s}, 0.1 \text{ s}]$, the second-order accurate implicit three-point backward difference scheme is used for time integration, and the computational time-step size is fixed to $\Delta t = 8 \times 10^{-5} \text{ s}$. For the chosen CFD mesh, this time-step size corresponds to a maximum CFL number of roughly 2000. The nonlinear system of algebraic equations arising at each time step is solved by Newton's method. Convergence is declared at the k -th iteration for the n -th time step when the residual satisfies $\|R^{n(k)}\| \leq 0.001\|R^{n(0)}\|$. All flow computations are performed in a non-dimensional setting.

A steady-state simulation computes the initial condition for the unsteady simulation. This steady-state calculation is characterized by the same parameters as above, except that it employs local time stepping

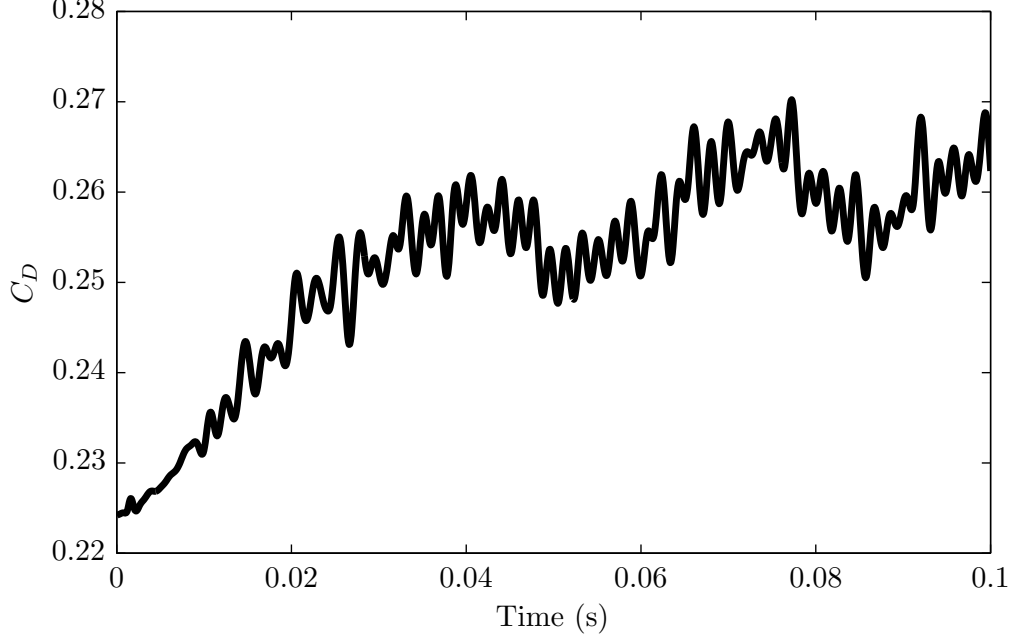


Figure 6 Time history of the drag coefficient predicted for $\varphi = 20^\circ$ using DES and a CFD mesh with $N = 17,342,604$ unknowns. Oscillatory behavior due to vortex shedding is apparent.

with a maximum CFL number of 50, it uses the first-order implicit backward Euler time integration scheme, and it employs only one Newton iteration per (pseudo) time step.

All computations are performed in double-precision arithmetic on a parallel Linux cluster² using a variable number of cores.

6.2.3. Comparison with experiment

Ref. [41] reports an experimental drag coefficient of 0.250 around the Ahmed body for a slant angle of $\varphi = 20^\circ$. Figure 6 reports the time history of the drag coefficient computed using the high-dimensional CFD model described in the previous section. Indeed, the time-averaged value of the computed drag coefficient obtained using the trapezoidal rule is $C_D = 0.2524$. Hence, it is within less than 1% of the reported experimental value. This asserts the quality of the constructed CFD model and AERO-F's computations. For reference, this high-dimensional CFD simulation consumed 13.28 hours on 512 cores.

6.2.4. ROM performance metrics

The following metrics will be used to assess GNAT's performance. The relative discrepancy in the drag coefficient, which assesses the accuracy of a GNAT simulation, is measured as follows:

$$\text{RD} = \frac{\frac{1}{n_t} \sum_{n=1}^{n_t} |C_{D_I}^n - C_{D_{III}}^n|}{\max_n C_{D_I}^n - \min_n C_{D_I}^n}, \quad (28)$$

where $C_{D_I}^n$ denotes the drag coefficient computed at the n -th time step using the high-dimensional CFD model (tier I model), and $C_{D_{III}}^n$ denotes the corresponding value computed using the GNAT ROM (tier III model).

²The cluster contains compute nodes with 16 GB of memory. Each node consists of two quad-core Intel Xeon E5345 processors running at 2.33 GHz inside a DELL Poweredge 1950. The interconnect is Cisco DDR InfiniBand.

The improvement in CPU performance delivered by GNAT as measured in wall time is defined as

$$\text{WT} = \frac{T_I}{T_{III}}, \quad (29)$$

where T_I denotes the wall time consumed by a flow simulation associated with the high-dimensional CFD model, and T_{III} denotes the wall time consumed *online* by its counterpart based on a GNAT ROM. For the high-dimensional model, the reported wall time includes the solution of the governing equations and the output of the state vector; for the GNAT reduced-order model, it includes the execution of Algorithm 1. After the completion of Algorithm 1, Algorithm 2 is executed to compute the drag coefficient. This output-computation step employs a sample mesh based on nodes \mathcal{K} determined from the wet surface; it is characterized by 124,047 nodes and 492,445 tetrahedral cells. For all reduced-order models, Algorithm 2 consumed 12.2 minutes on 4 cores, or 9.7 minutes on 8 cores.

The improvement in CPU performance delivered by GNAT as measured in computational resources is defined as

$$\text{CR} = \frac{c_I T_I}{c_{III} T_{III}}, \quad (30)$$

where c_I and c_{III} denote the number of cores allocated to the high-dimensional and GNAT-ROM simulations, respectively.

As reported in Section 6.2.3, the high-dimensional CFD simulation is characterized by $T_I = 13.28$ hours and $c_I = 512$ cores, which leads to $c_I T_I = 6,798$ core-hours.

6.2.5. GNAT performance assessment

This section assesses GNAT's performance for two different snapshot-collection procedures: procedures 0 and 1 of Table 1. Recall from Section 3.4.2 that snapshot-collection procedure 0 is inconsistent in the sense introduced in Ref. [1] and restated in Section 3.1, but is similar to the approach most often taken in the literature. Procedure 1 satisfies one consistency condition. Procedure 2 is not tested because Ref. [46] showed that it does not lead to robust reduced-order models; procedure 3 is not tested due to computational infeasibility.

To build the state POD basis, consistent snapshots $\{w^n - w^0\}_{n=1}^{n_t}$ with $n_t = 1252$ are collected during high-dimensional CFD simulation. Then, these snapshots are normalized to prevent snapshots with large magnitudes from biasing the SVD. The dimension of the state POD basis is set to $n_w = 283$, which corresponds to 99.99% of the total statistical energy of the (normalized) snapshots.³ All numerical studies carried out on the Ahmed body employ this POD basis for the state.

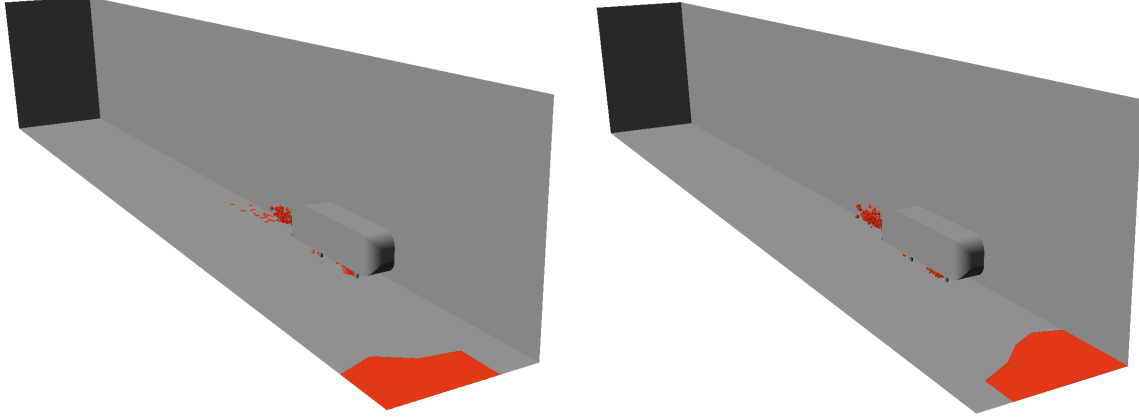
Algorithm 3 is employed to generate two sample meshes: one using the matrix $\Phi_R = \Phi_J$ generated by snapshot-collection procedure 0, and one using $\Phi_R = \Phi_J$ generated by snapshot-collection procedure 1.⁴ This algorithm employs the following parameters: $n_c = 219$, $n_s = 378$, and an initial sample-node set \mathcal{N} seeded with the boundary node whose entries of ϕ_R^1 have the largest sum of squares. Figure 7 depicts the two resulting sample meshes. Note that Algorithm 3 chooses sample nodes from three salient regions of the computational fluid domain: the wake region behind the body, and the region behind each cylindrical support. This implies that on average, the magnitude of the residual is highest in these regions during the training simulations. This is consistent with the fact that the flow is separated in these regions and is characterized by a strong vorticity.

The two GNAT models employ $n_J = n_R = 1514$; this corresponds to 99.99% of the energy in the snapshots of the residual collected during the tier II ROM simulation. Both GNAT simulations are executed using only 4 cores (as compared with 512 cores used for the high-dimensional model). The GNAT simulations employ the same Ahmed-body configuration and flow conditions used for the high-dimensional CFD simulation.

Figure 8 reports the time histories of the drag coefficient predicted by the high-dimensional simulation and both GNAT ROM computations. Figure 9 contrasts the surface pressure contours at $t = 0.1$ s obtained

³Numerical experiments reported in Ref. [46] determined this to be an appropriate criterion.

⁴Residual snapshots are normalized before Φ_R is computed.



(a) Sample mesh generated using snapshot-collection procedure 0 (b) Sample mesh generated using snapshot-collection procedure 1

Figure 7 Sample meshes with 378 sample nodes generated by Algorithm 3. Sample meshes are shown in red, within the computational fluid domain.

Table 3 Online performance results of GNAT on 4 cores for a sample mesh with 378 sample nodes

Snapshot-collection procedure	RD	Average # of Newton iterations per time step	Wall time (hours)	CR	WT
0	7.43%	6.47	7.37	231	1.80
1	0.68%	2.75	3.88	438	3.42

using the high-dimensional model and the GNAT ROM based on snapshot-collection procedure 1. Table 3 provides the performance results for the ROM simulations. These results demonstrate the following:

- Both snapshot-collection procedures 0 and 1 lead to GNAT ROMs that deliver improvement in CPU performance (as measured in computational resources CR) exceeding 230. This occurs largely due to the drastic reduction in cores made possible by the sample-mesh implementation, which allows the ROM simulation to be executed on as few as 4 cores. In particular, the data suggest that 438 parametric GNAT ROM simulations (using snapshot-collection procedure 1) could be executed in a predictive scenario using the same core-hours required by a single high-dimensional CFD computation (see Table 3)— a test that will be conducted in the future.
- When equipped with snapshot-collection procedure 1, which satisfies one consistency condition, the GNAT ROM reproduces almost perfectly the time history of the drag coefficient computed by the high-dimensional simulation. On the other hand, GNAT becomes less accurate when equipped with snapshot-collection procedure 0, which is inconsistent (see Figure 8). Furthermore, GNAT requires fewer Newton iterations per time step for convergence (and performs faster) when it is equipped with snapshot-collection procedure 1 compared with snapshot-collection procedure 0 (see Table 3). These observations highlight the importance of the consistency concept introduced during GNAT’s development.
- When equipped with snapshot-collection procedure 1, GNAT delivers pressure-contour results that are almost identical to those computed by the high-dimensional simulation, including in the wake region behind the body where the flow is most complex (see Figure 9).

6.2.6. Effect of node sampling and interpolation vs. least-squares approximation

To illustrate the effect of the number of sample nodes on GNAT’s performance, this study considers three sample meshes: the sample mesh with 378 sample nodes introduced above (constructed using snapshot-

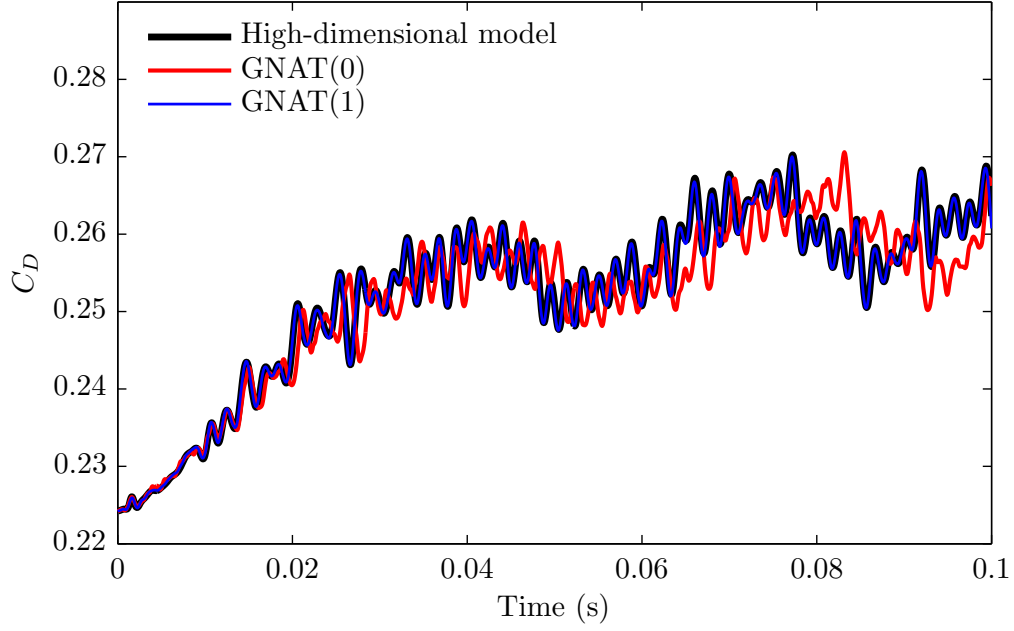


Figure 8 Computed time histories of the drag coefficient (GNAT(i) refers to GNAT equipped with snapshot-collection procedure i). GNAT(1) directly overlays the high-dimensional model results.

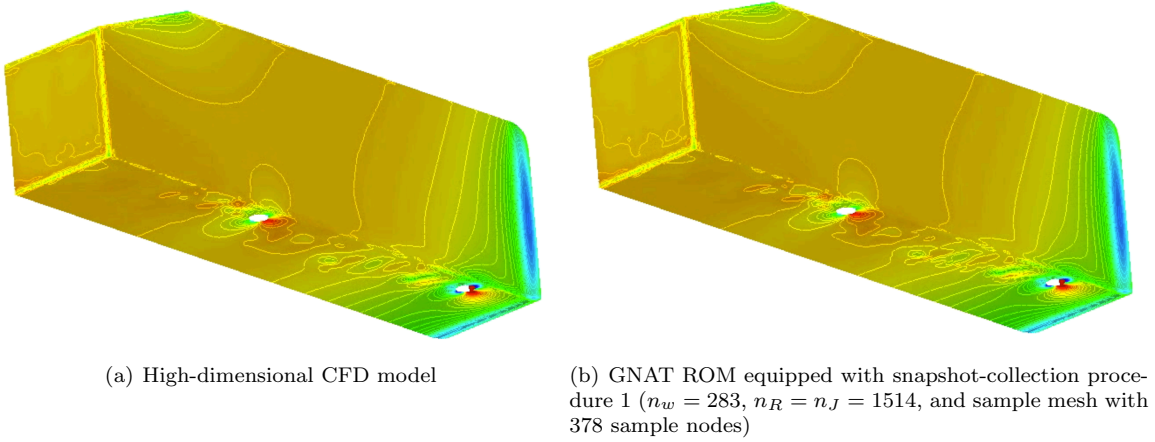


Figure 9 Surface-pressure contours at $t = 0.1$ s

Table 4 Sample-mesh attributes

# of sample nodes	# of nodes	# of elements	Fraction of nodes of original CFD mesh	Fraction of elements of original CFD mesh
253	12808	41014	0.44%	0.24%
378	17096	56280	0.59%	0.33%
505	19822	67082	0.69%	0.39%

collection procedure 1), a smaller sample mesh with 253 sample nodes, and a larger one with 505 sample nodes. Algorithm 3 is executed to generate these sample meshes; it employs parameters $n_c = 219$ and $\Phi_R = \Phi_J$ generated by snapshot-collection procedure 1. Table 4 reports the characteristics of these sample meshes. The GNAT models for these simulations are equipped with snapshot-collection procedure 1 and employ $n_J = n_R = 1514$ as in the previous section. Because $\nu = 6$, the hyper-reduction associated with 253 sample nodes corresponds roughly to interpolation of the residual and its Jacobian. Indeed, the sample-index factor in this case is $\eta = (253 \times 6)/1514 \approx 1$. For the case of 378 sample nodes, $\eta = 1.5$; the sample mesh with 505 sample nodes is characterized by $\eta = 2.0$. These latter two cases correspond to least-squares approximation of the residual and its Jacobian.

Figure 10 reports the time histories of the drag coefficient obtained using the high-dimensional model and the GNAT ROMs based on these three sample meshes. Table 5 provides the performance results for the ROM simulations obtained using 4 cores. These results indicate the following:

- In all cases, GNAT reproduces the time history of the drag coefficient computed using the high-dimensional model with less than 1% discrepancy.
- As sample nodes are added, the convergence of Newton’s method at each time step improves on average.
- The fastest performance of GNAT is obtained for the smallest sample mesh.
- Interpolation of the residual and its Jacobian (253 sample nodes) does not lead to the best convergence of the Newton solver or the most accurate results. However, it does lead to the best overall CPU performance of GNAT in this case.

Table 5 Online performance on 4 cores of GNAT equipped with snapshot-collection procedure 1 for various sample meshes

# of sample nodes	η	RD	Average # of Newton iterations per time step	Wall time (hours)	CR	WT
253	≈ 1	0.79%	4.38	3.77	452	3.52
378	1.5	0.68%	2.75	3.88	438	3.42
505	2.0	0.75%	2.25	4.22	403	3.15

6.2.7. Parallel scalability

Due to the sample mesh concept, GNAT is parallelized in the same manner as a typical CFD code is, using mesh partitioning. However, because GNAT operates on a dramatically smaller mesh, its parallel performance cannot be expected to scale in the strong sense — that is, for a fixed ROM size and an increasing number of processors. This is also true for the online stage of any other model-reduction method.

To obtain an idea of the strong scaling that can be expected from a nonlinear model-reduction method, Table 6 reports the CPU performance results obtained for GNAT equipped with snapshot-collection procedure 1, the sample mesh with 378 sample nodes, and $n_J = n_R = 1514$. Excellent speedups are obtained for a number of cores varying between 2 and 8, a good speedup is obtained for 12 cores, and a reasonable one is obtained for 16 cores. For a larger number of cores, the parallel efficiency (defined as the ratio of the speedup to the number of cores) increasingly deteriorates. This is not surprising given that the GNAT ROM operates on a mesh with only 378 sample nodes.

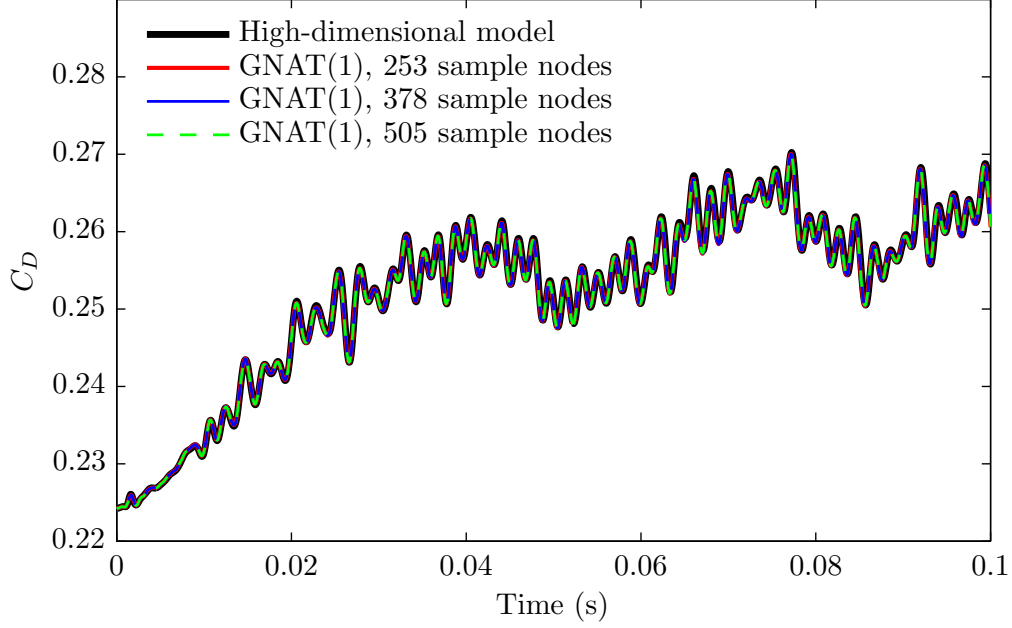


Figure 10 Computed time histories of the drag coefficient for different numbers of sample nodes (GNAT(1) refers to GNAT equipped with snapshot-collection procedure 1)

Table 6 Assessment of GNAT’s strong scaling performance for a sample mesh with 378 sample nodes

# of cores	Wall time (hours)	Speedup	WT	CR
1	16.1	1.0	0.83	422
2	8.74	1.84	1.52	388
4	3.88	4.14*	3.43	438
8	2.50	6.44	5.32	340
12	1.94	8.25	6.86	292
16	2.08	7.74	6.39	204

*This superlinear speedup is likely due to caching and other memory management effects.

6.2.8. Performance comparison with other function-sampling ROM methods

To conclude this section, the performance of GNAT equipped with snapshot-collection procedure 1 and $n_J = n_R = 1514$ is compared to that of other hyper-reduction techniques based on function sampling. This study employs the same wake flow problem, the same state POD basis of dimension $n_w = 283$, and same sample mesh with 378 sample nodes. The following function-sampling techniques are compared with GNAT:

1. A collocation of the nonlinear equations followed by a Galerkin projection of the resulting over-determined system of 2268 nonlinear equations (378 sample nodes \times 6 equations per node) with $n_w = 283$ unknowns [29, 20].
2. A collocation followed by a least-squares solution of the resulting over-determined system [28].
3. A discrete empirical interpolation method (DEIM)-like [31] approach that employs snapshot-collection procedure 0 and $n_R = n_J = 2268$ so that the residual and Jacobian functions are approximated by interpolation. The tested approach employs the tier II Petrov–Galerkin solution of the overdetermined equations as opposed to the Galerkin projection; this is done to isolate the effect of the hyper-reduction technique on performance.

Figure 11 reports the time histories of the drag-coefficient computed using all hyper-reduction techniques outlined above. Both collocation approaches lead to nonlinear instabilities after a few time steps of the flow simulation, thereby exposing the weakness of collocation for highly nonlinear problems. The DEIM-like approach, which employs the popular but inconsistent snapshot-collection procedure 0, also performs poorly. For this approach, the Newton iterations begin to generate zero search directions after only a few time steps of the flow simulation.

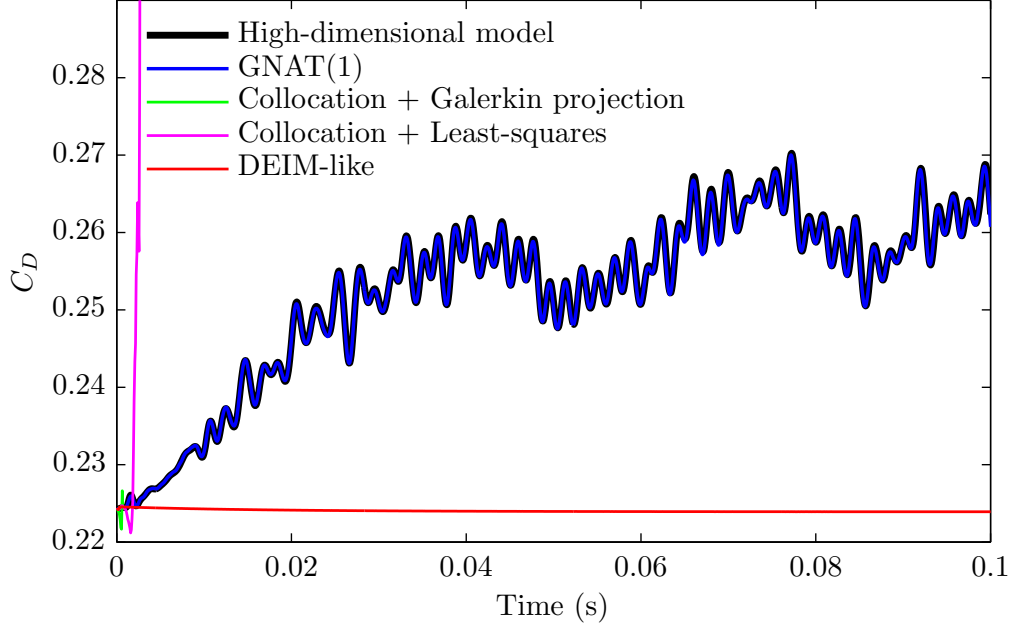


Figure 11 Computed time histories of the drag coefficient (GNAT(1) refers to GNAT equipped with snapshot-collection procedure 1)

7. Conclusions

In this work, the Gauss–Newton with approximated tensors (GNAT) nonlinear model-reduction method is equipped with a sample-mesh concept that eases the implementation of its online stage on parallel computing platforms. This work also develops global state-space error bounds that justify GNAT’s design, characterize its mathematical properties, and highlight its advantages in terms of minimizing components of these bounds. The effectiveness of GNAT on parametric problems and its robustness for highly nonlinear computational fluid dynamics (CFD) applications characterized by moving shocks is demonstrated by the solution of a conservation problem described by the inviscid Burgers’ equation with a variable source term and boundary condition. GNAT’s ability to reduce by orders of magnitude the core-hours required to compute turbulent viscous flows at high Reynolds numbers, while preserving accuracy, is demonstrated with the simulation of the flow field in the wake of the Ahmed body. For this popular benchmark problem with over 17 million unknowns, GNAT is found to outperform several other nonlinear model reduction methods, reduce the required computational resources by more than two orders of magnitude, and deliver a solution with less than 1% discrepancy compared to its high-dimensional counterpart.

Appendix A. Proof of consistent snapshots for the state POD basis

The following proposition proves that two options for collecting state snapshots lead to a consistent projection. For the sake of simplicity, one set of training inputs μ^{train} is considered and therefore $\mathcal{D}_{\text{train}} =$

$\{\mu^{\text{train}}\}$. Recall the reduced-order-model solution is defined by Eq. (6) as

$$\tilde{w}^n(\mu) = w^0(\mu) + \Phi_w w_r^n(\mu), \quad n = 0, \dots, n_t. \quad (\text{A.1})$$

Proposition Appendix A.1. Consistency of the state snapshots. Assume the following:

1. The set of snapshots W_1 or W_2 is used to compute Φ_w via POD, where

$$W_1 \equiv \{w^n(\mu^{\text{train}}) - w^0(\mu^{\text{train}}) \mid n = 1, \dots, n_t\} \quad (\text{A.2})$$

$$W_2 \equiv \{w^n(\mu^{\text{train}}) - w^{n-1}(\mu^{\text{train}}) \mid n = 1, \dots, n_t\}. \quad (\text{A.3})$$

2. The Gauss–Newton method is employed to compute solutions $w_r^{n+1}(\mu)$ to the nonlinear least-squares problem

$$w_r^{n+1}(\mu) = \arg \min_{y \in \mathbb{R}^{n_w}} f^n(y; \mu), \quad (\text{A.4})$$

for $n = 0, \dots, n_t - 1$ and any $\mu \in \mathcal{D}$. Here,

$$f^n(y; \mu) \equiv \frac{1}{2} \|\tilde{R}^n(w^0(\mu) + \Phi_w y; \mu)\|_2^2. \quad (\text{A.5})$$

The residual \tilde{R}^n arising from the sequence of reduced-order-model solutions is related to the residual R^n arising from the sequence of high-dimensional-model solutions as follows:

$$\tilde{R}^n(w; \mu) \equiv S^n(w, \tilde{w}^n, \dots, \tilde{w}^1, w^0; \mu) \quad (\text{A.6})$$

$$S^n(w, w^n, \dots, w^1, w^0; \mu) \equiv R^n(w; \mu), \quad (\text{A.7})$$

for $n = 0, \dots, n_t - 1$ and any $\mu \in \mathcal{D}$. Here, S^n explicitly reflects the dependence of the residual on the state at previous time steps.

3. The reduced-order model employs the same initial condition as the high-dimensional model:

$$w_r^0(\mu) = 0. \quad (\text{A.8})$$

4. The standard assumptions (see Theorem 10.1 [47]) needed for the convergence of the Gauss–Newton iterations to a stationary point contained in the level set $\mathcal{L}^n(\mu)$:

$$w_r^{n+1}(\mu) \in \mathcal{M}^n(\mu), \quad (\text{A.9})$$

for $n = 0, \dots, n_t - 1$ and any $\mu \in \mathcal{D}$. Here, define

$$\mathcal{L}^n(\mu) \equiv \{y \mid f^n(y; \mu) \leq f^n(w_r^{n+1(0)}; \mu)\} \quad (\text{A.10})$$

$$\mathcal{M}^n(\mu) \equiv \{y \mid y \in \mathcal{L}^n(\mu), \nabla f^n(y; \mu) = 0\}. \quad (\text{A.11})$$

5. The level set $\mathcal{L}^n(\mu)$ contains only one stationary point: $|\mathcal{M}^n(\mu)| = 1$ for $n = 0, \dots, n_t - 1$ and any $\mu \in \mathcal{D}$.

Then, the projection approximation is consistent in the sense that the Petrov–Galerkin ROM (i.e., GNAT without hyper-reduction) associated with a POD basis Φ_w that is not truncated computes the same states as the original high-dimensional CFD model for the training inputs — that is,

$$\tilde{w}^n(\mu^{\text{train}}) = w^n(\mu^{\text{train}}), \quad n = 0, \dots, n_t. \quad (\text{A.12})$$

Proof: Consider computing solutions $\tilde{w}^n(\mu^{\text{train}})$, $n = 0, \dots, n_t$ under the stated assumptions. In the sequel, the argument μ^{train} is dropped for notational simplicity. The result, i.e., Eq. (A.12), is proven by induction. It is true for $n = 0$ due to Assumption 3. Assume now that $\tilde{w}^i = w^i$, $i = 0, \dots, n$.

Assumption 2 ensures that the Gauss–Newton method is used to compute the solution w_r^{n+1} . Assumption 4 guarantees that these Gauss–Newton iterations will converge to a local stationary point in the level set \mathcal{L}^n . Therefore,

$$w_r^{n+1} \in \mathcal{M}^n. \quad (\text{A.13})$$

Assumption 1 ensures that

$$w^{n+1} - w^0 \in \text{range}(\Phi_w). \quad (\text{A.14})$$

To see this, first consider the case where \mathbf{W}_1 is used to compute Φ_w . Then, $w^{n+1}(\mu^{\text{train}}) - w^0(\mu^{\text{train}}) \in \mathbf{W}_1$ and therefore $w^{n+1}(\mu^{\text{train}}) - w^0(\mu^{\text{train}}) \in \text{span}(\mathbf{W}_1)$. If the POD basis Φ_w is not truncated, then $\text{range}(\Phi_w) = \text{span}(\mathbf{W}_1)$ and Eq. (A.14) holds. Now, consider the case where \mathbf{W}_2 is used for computing Φ_w . Because $w^{i+1}(\mu^{\text{train}}) - w^i(\mu^{\text{train}}) \in \mathbf{W}_2$, $i = 0, \dots, n_t$, then $w^{n+1}(\mu^{\text{train}}) - w^0(\mu^{\text{train}}) \in \text{span}(\mathbf{W}_2)$. If the POD basis Φ_w is not truncated, then $\text{range}(\Phi_w) = \text{span}(\mathbf{W}_2)$, and again Eq. (A.14) holds.

The induction assumption ($\tilde{w}^i = w^i$, $i = 0, \dots, n$) and Eq. (A.14) ensure that

$$\Phi_w^T(w^{n+1} - w^0) \in \mathcal{M}^n. \quad (\text{A.15})$$

This can be derived by setting $y = \Phi_w^T(w^{n+1} - w^0)$ and writing the objective function:

$$f^n(\Phi_w^T(w^{n+1} - w^0)) = \frac{1}{2} \|\tilde{R}^n(w^0 + \Phi_w \Phi_w^T(w^{n+1} - w^0))\|_2^2 \quad (\text{A.16})$$

$$= \frac{1}{2} \|\tilde{R}^n(w^{n+1})\|_2^2 \quad (\text{A.17})$$

$$= \frac{1}{2} \|R^n(w^{n+1})\|_2^2 \quad (\text{A.18})$$

$$= 0. \quad (\text{A.19})$$

Eq. (A.17) is due to Eq. (A.14) and the orthogonality of the POD basis. Eq. (A.18) arises from the equalities

$$\tilde{R}^n(w) = S^n(w, \tilde{w}^n, \dots, \tilde{w}^1, w^0) = S^n(w, w^n, \dots, w^1, w^0) = R^n(w), \quad (\text{A.20})$$

which hold due to the induction assumption. Finally, Eq. (A.19) holds because the full-order solution leads to a zero residual: $R^n(w^{n+1}) = 0$. Because $f^n(y) \geq 0 \forall y$, Eq. (A.19) implies that $\Phi_w^T(w^{n+1} - w^0)$ is a local minimizer of f^n , so Eq. (A.15) holds.

Assumption 5, Eq. (A.13), and Eq. (A.15) together imply

$$w_r^{n+1} = \Phi_w^T(w^{n+1} - w^0). \quad (\text{A.21})$$

Substituting Eq. (A.21) into Eq. (A.1) yields

$$\tilde{w}^{n+1} = w^0 + \Phi_w \Phi_w^T(w^{n+1} - w^0). \quad (\text{A.22})$$

Eq. (A.22) along with Eq. (A.14) and the orthogonality of the POD basis provides the result:

$$\boxed{\tilde{w}^{n+1}(\mu^{\text{train}}) = w^{n+1}(\mu^{\text{train}}), \quad n = 0, \dots, n_t.} \quad (\text{A.23})$$

□

Appendix B. Further discussion of the various snapshot-collection procedures

If $\Phi_J = \Phi_R$, then $A = B$ and $BZJ^{(k)}\Phi_w = \frac{\partial[BZR(w^{(0)} + \Phi_w y)]}{\partial y}$. As a result, the GNAT iterations (15)–(16) are in this case equivalent to the Gauss–Newton iterations for solving

$$\underset{\bar{w} \in w^{(0)} + \mathcal{W}}{\text{minimize}} \|BZR(\bar{w})\|_2. \quad (\text{B.1})$$

Because $\|BZR\|_2 = \|\Phi_R BZR\|_2$ when $\Phi_R^T \Phi_R = I$ and the gappy POD approximation of R is $\tilde{R} = \Phi_R BZR$, the GNAT iterations are also equivalent to the Gauss–Newton iterations for solving

$$\underset{\bar{w} \in w^{(0)} + \mathcal{W}}{\text{minimize}} \|\tilde{R}(\bar{w})\|_2. \quad (\text{B.2})$$

Therefore, when $\Phi_J = \Phi_R$ and Φ_R has orthonormal columns, GNAT inherits the convergence properties of the Gauss–Newton method. This is the rationale behind both procedure 0 and procedure 1 outlined in Section 3.4.2.

On the other hand, procedure 2 and procedure 3 use different bases Φ_R and Φ_J . For this reason, the GNAT iterations (15)–(16) cannot be associated with Gauss–Newton iterations for nonlinear residual minimization. Furthermore, choosing $\Phi_J \neq \Phi_R$ causes the least-squares problem (15) to try to ‘match’ quantities that lie in different subspaces. For these reasons, procedure 2 and procedure 3 may lack robustness and experience convergence difficulties as reported in Ref. [46].

Appendix C. Error bounds for the solution computed by a discrete nonlinear model reduction method

This section proves the error bound (22) presented in Section 4. For the sake of notational simplicity, the derivation presented here considers the approximation error arising from a given set of inputs and therefore omits μ from the arguments of the nonlinear functions. Rewriting the residual (19) in this fashion leads to

$$R^n(w^{n+1}) = w^{n+1} - w^n - \Delta t F(w^{n+1}, t^{n+1}). \quad (\text{C.1})$$

Similarly, the residual at the the n -th time step arising from any sequence of approximate solutions \tilde{w}^n , $n = 0, \dots, n_t$, e.g., generated by a discrete nonlinear ROM, for the same input parameters can be written as

$$\tilde{R}^n(\tilde{w}^{n+1}) = \tilde{w}^{n+1} - \tilde{w}^n - \Delta t F(\tilde{w}^{n+1}, t^{n+1}). \quad (\text{C.2})$$

Subtracting (C.2) from (C.1) yields

$$R^n(w^{n+1}) - \tilde{R}^n(\tilde{w}^{n+1}) = w^{n+1} - w^n - \Delta t F(w^{n+1}, t^{n+1}) - \tilde{w}^{n+1} + \tilde{w}^n + \Delta t F(\tilde{w}^{n+1}, t^{n+1}). \quad (\text{C.3})$$

The above expression can be re-arranged as

$$w^{n+1} - \tilde{w}^{n+1} - \Delta t F(w^{n+1}, t^{n+1}) + \Delta t F(\tilde{w}^{n+1}, t^{n+1}) = R^n(w^{n+1}) - \tilde{R}^n(\tilde{w}^{n+1}) + w^n - \tilde{w}^n. \quad (\text{C.4})$$

Introducing $f : (x, t) \mapsto x - \Delta t F(x, t)$ and the inverse Lipschitz constant⁵

$$\mathcal{L}_G^n \equiv \sup_{x \neq y} \frac{\|x - y\|}{\|f(x, t^{n+1}) - f(y, t^{n+1})\|} \quad (\text{C.5})$$

allows Eq. (C.4) to be transformed into the following bound on the *local* approximation error:

$$\|w^{n+1} - \tilde{w}^{n+1}\| \leq \mathcal{L}_G^n \left(\epsilon_{\text{Newton}} + \|\tilde{R}^n(\tilde{w}^{n+1})\| + \|w^n - \tilde{w}^n\| \right). \quad (\text{C.6})$$

⁵Note that $\epsilon = \frac{1}{\mathcal{L}_G^n}$ in Eq. (20).

Assuming that the initial approximation error is zero⁶ ($\tilde{w}^0 = w^0$), the inequality (C.6) leads to the following result

$$\|w^n - \tilde{w}^n\| \leq \sum_{k=1}^n a^k b_{n-k}, \quad (\text{C.7})$$

where $a = \mathcal{L}_G \equiv \sup_{n \in \{1, \dots, n_t\}} \mathcal{L}_G^n$ and

$$b_n \equiv \epsilon_{\text{Newton}} + \|\tilde{R}^n(\tilde{w}^{n+1})\|. \quad (\text{C.8})$$

From the triangle inequality, it follows that $\|\tilde{R}^n(\tilde{w}^{n+1})\| \leq \|P\tilde{R}^n(\tilde{w}^{n+1})\| + \|(I - P)\tilde{R}^n(\tilde{w}^{n+1})\|$ for any P . Hence, another bound for the approximation error is

$$\|w^n - \tilde{w}^n\| \leq \sum_{k=1}^n a^k c_{n-k}, \quad (\text{C.9})$$

where

$$c_n \equiv \epsilon_{\text{Newton}} + \|P\tilde{R}^n(\tilde{w}^{n+1})\| + \|(I - P)\tilde{R}^n(\tilde{w}^{n+1})\| \quad (\text{C.10})$$

and $c_n \geq b_n$. The bound (C.9) is particularly interesting for the case where $P = \Phi_R [Z\Phi_R]^+ Z$ represents the gappy POD operator because $\|P\tilde{R}^n(\tilde{w}^{n+1})\| = \|[Z\Phi_R]^+ Z\tilde{R}^n(\tilde{w}^{n+1})\|$ is readily computable by GNAT.

In Appendix D, it is shown that an upper bound for the gappy POD approximation error is

$$\|(I - P)\tilde{R}^n(\tilde{w}^{n+1})\| \leq \|R^{-1}\| \|(I - \mathbb{P})\tilde{R}^n(\tilde{w}^{n+1})\|, \quad (\text{C.11})$$

where $\mathbb{P} = \Phi_R \Phi_R^T$ defines the orthogonal projector onto range(Φ_R), and $Z\Phi_R = QR$ is the thin QR factorization of $Z\Phi_R$ with $Q \in \mathbb{R}^{n_i \times n_R}$ and $R \in \mathbb{R}^{n_R \times n_R}$. Therefore from (C.11), it follows that yet another error bound for the approximation error is

$$\|w^n - \tilde{w}^n\| \leq \sum_{k=1}^n a^k d_{n-k}, \quad (\text{C.12})$$

where

$$d_n \equiv \epsilon_{\text{Newton}} + \|P\tilde{R}^n(\tilde{w}^{n+1})\| + \|R^{-1}\| \|(I - \mathbb{P})\tilde{R}^n(\tilde{w}^{n+1})\|. \quad (\text{C.13})$$

Because $b_n \leq c_n \leq d_n$, it follows that a global bound for the approximation error at the n -th time step with $1 \leq n \leq n_t$ is given by

$$\boxed{\|w^n - \tilde{w}^n\| \leq \sum_{k=1}^n a^k b_{n-k} \leq \sum_{k=1}^n a^k c_{n-k} \leq \sum_{k=1}^n a^k d_{n-k}.} \quad (\text{C.14})$$

Appendix D. Error bound for the gappy POD approximation

This section establishes a bound for the error associated with the gappy POD approximation of a vector $g \in \mathbb{R}^N$ using a POD basis $\Phi_f \in \mathbb{R}^{N \times n_f}$ and a set of $n_i \geq n_f$ sample indices \mathcal{I} that define the sample matrix Z (see Section 3.4.1 for these definitions).⁷

Define $g^* \equiv \mathbb{P}g$ with $\mathbb{P} \equiv \Phi_f \Phi_f^T$ as the orthogonal (i.e., optimal) projection of g onto range(Φ_f). Also, define the difference between g and its orthogonal projection onto range(Φ_f) as $e \equiv g - g^*$. Finally, define the gappy POD projection matrix $P \equiv \Phi_g R^{-1} Q^T Z$, where $Z\Phi_f = QR$ is the thin QR factorization of $Z\Phi_f$ with $Q \in \mathbb{R}^{n_i \times n_f}$ and $R \in \mathbb{R}^{n_f \times n_f}$.

⁶This is valid for both the Petrov–Galerkin and GNAT ROMs as they employ the same initial condition as the high-dimensional model (See Algorithm 1).

⁷This development follows closely the proof of Lemma 3.2 in Ref. [31].

The gappy POD approximation of g is $Pg = P(e + g^*)$. It can also be written as

$$Pg = Pe + g^* \quad (\text{D.1})$$

because $Pg^* = g^*$, as $g^* \in \text{range}(\Phi_f)$. Substituting $g^* = g - e$ into Eq. (D.1) yields $(I - P)g = (I - P)e$. Therefore,

$$\|(I - P)g\|_2 = \|(I - P)e\|_2 \leq \|(I - P)\|_2 \|e\|_2. \quad (\text{D.2})$$

Because $\|I - P\|_2 = \|P\|_2$ for any projection matrix P not equal to 0 or I , it follows that

$$\|I - P\|_2 = \|P\|_2 = \|\Phi_g R^{-1} Q^T Z\|_2 = \|R^{-1}\|_2. \quad (\text{D.3})$$

The last equality follows from the fact that Φ_g , Z^T , and Q have orthonormal columns. Substituting (D.3) in (D.2) gives the result

$$\|(I - P)g\|_2 \leq \|R^{-1}\|_2 \|(I - \mathbb{P})g\|_2. \quad (\text{D.4})$$

Acknowledgments

Most of this work was completed while the first and third authors were at Stanford University. The authors thank Phil Avery and Charbel Bou-Mosleh for their contributions to the parallel implementation of GNAT in AERO-F, and Matthew Zahr for his contribution to the Burgers' equation example. All authors acknowledge partial support by the Motor Sports Division of the Toyota Motor Corporation under Agreement Number 48737, and partial support by the Army Research Laboratory through the Army High Performance Computing Research Center under Cooperative Agreement W911NF-07-2-0027. The first author also acknowledges partial support by the National Science Foundation Graduate Fellowship, the National Defense Science and Engineering Graduate Fellowship, and an appointment to the Sandia National Laboratories Truman Fellowship in National Security Science and Engineering. The Truman Fellowship is sponsored by Sandia Corporation (a wholly owned subsidiary of Lockheed Martin Corporation) as Operator of Sandia National Laboratories under its U.S. Department of Energy Contract No. DE-AC04-94AL85000. The content of this publication does not necessarily reflect the position or policy of any of these institutions, and no official endorsement should be inferred.

References

- [1] K. Carlberg, C. Bou-Mosleh, C. Farhat, Efficient non-linear model reduction via a least-squares Petrov–Galerkin projection and compressive tensor approximations, *International Journal for Numerical Methods in Engineering* 86 (2011) 155–181.
- [2] A. C. Antoulas, *Approximation of Large-Scale Dynamical Systems*, Society for Industrial and Applied Mathematics, Philadelphia, PA, 2005.
- [3] D. Amsallem, J. Cortial, K. Carlberg, C. Farhat, A method for interpolating on manifolds structural dynamics reduced-order models, *International Journal for Numerical Methods in Engineering* 80 (2009) 1241–1258.
- [4] C. Prud'homme, D. V. Rovas, K. Veroy, L. Machiels, Y. Maday, A. T. Patera, G. Turinici, Reliable real-time solution of parameterized partial differential equations: Reduced-basis output bound methods, *Journal of Fluids Engineering* 124 (2002) 70–80.
- [5] G. Rozza, D. B. P. Huynh, A. T. Patera, Reduced basis approximation and a posteriori error estimation for affinely parametrized elliptic coercive partial differential equations, *Archives of Computational Methods in Engineering* 15 (2008) 229–275.

- [6] K. Veroy, C. Prud'homme, D. V. Rovas, A. T. Patera, A posteriori error bounds for reduced-basis approximation of parametrized noncoercive and nonlinear elliptic partial differential equations, AIAA Paper 2003-3847, 16th AIAA Computational Fluid Dynamics Conference, Orlando, FL (2003).
- [7] N. C. Nguyen, K. Veroy, A. T. Patera, Certified real-time solution of parametrized partial differential equations, Kluwer Academic Publishing, Dordrecht, pp. 1529–1564.
- [8] K. Veroy, A. T. Patera, Certified real-time solution of the parametrized steady incompressible Navier-Stokes equations: Rigorous reduced-basis a posteriori error bounds, International Journal for Numerical Methods in Fluids 47 (2005) 773–788.
- [9] K. C. Hall, J. P. Thomas, E. H. Dowell, Reduced-order modelling of unsteady small-disturbance flows using a frequency domain proper orthogonal decomposition technique, in: AIAA Paper 99-16520.
- [10] P. A. LeGresley, J. J. Alonso, Airfoil design optimization using reduced order models based on proper orthogonal decomposition, in: AIAA Paper 2000-25450, Fluids 2000 Conference and Exhibit, Denver, CO.
- [11] K. C. Hall, J. P. Thomas, E. H. Dowell, Proper orthogonal decomposition technique for transonic unsteady aerodynamic flows, AIAA Journal 38 (2000) 1853–1862.
- [12] W. K., J. Peraire, Balanced model reduction via the proper orthogonal decomposition, AIAA Journal 40 (2002) 2323–2330.
- [13] B. I. Epureanu, A parametric analysis of reduced order models of viscous flows in turbomachinery, Journal of Fluids and Structures 17 (2003) 971–982.
- [14] J. P. Thomas, E. H. Dowell, K. C. Hall, Three-dimensional transonic aeroelasticity using proper orthogonal decomposition-based reduced order models, Journal of Aircraft 40 (2003) 544–551.
- [15] T. Kim, M. Hong, K. B. Bhatia, G. SenGupta, Aeroelastic model reduction for affordable computational fluid dynamics-based flutter analysis, AIAA Journal 43 (2005) 2487–2495.
- [16] T. Lieu, C. Farhat, M. Lesoinne, Reduced-order fluid/structure modeling of a complete aircraft configuration, Computer Methods in Applied Mechanics and Engineering 195 (2006) 5730–5742.
- [17] T. Lieu, C. Farhat, Adaptation of aeroelastic reduced-order models and application to an F-16 configuration, AIAA Journal 45 (2007) 1244–1269.
- [18] D. Amsallem, C. Farhat, An interpolation method for adapting reduced-order models and application to aeroelasticity, AIAA Journal 46 (2008) 1803–1813.
- [19] D. Amsallem, J. Cortial, C. Farhat, Toward real-time CFD-based aeroelastic computations using a database of reduced-order information, AIAA Journal 48 (2010) 2029–2037.
- [20] D. Ryckelynck, A priori hyperreduction method: an adaptive approach, Journal of Computational Physics 202 (2005) 346–366.
- [21] D. Amsallem, M. J. Zahr, C. Farhat, Nonlinear model order reduction based on local reduced-order bases, International Journal for Numerical Methods in Engineering doi: 10.1002/nme.4371 (2012).
- [22] M. Barrault, Y. Maday, N. C. Nguyen, A. T. Patera, An ‘empirical interpolation’ method: application to efficient reduced-basis discretization of partial differential equations, Comptes Rendus Mathématique Académie des Sciences 339 (2004) 667–672.
- [23] M. A. Grepl, Y. Maday, N. C. Nguyen, A. T. Patera, Efficient reduced-basis treatment of nonaffine and nonlinear partial differential equations, ESAIM-Mathematical Modelling and Numerical Analysis (M2AN) 41 (2007) 575–605.

- [24] N. C. Nguyen, J. Peraire, An efficient reduced-order modeling approach for non-linear parametrized partial differential equations, *International Journal for Numerical Methods in Engineering* 76 (2008) 27–55.
- [25] B. Haasdonk, M. Ohlberger, G. Rozza, A reduced basis method for evolution schemes with parameter-dependent explicit operators, *Electronic Transactions on Numerical Analysis* 32 (2008) 145–161.
- [26] B. Haasdonk, M. Ohlberger, Reduced basis method for explicit finite volume approximations of nonlinear conservation laws, in: *Proc. 12th International Conference on Hyperbolic Problems: Theory, Numerics, Application*.
- [27] M. J. Rewienski, A Trajectory Piecewise-Linear Approach to Model Order Reduction of Nonlinear Dynamical Systems, Ph.D. thesis, Massachusetts Institute of Technology, 2003.
- [28] P. A. LeGresley, Application of Proper Orthogonal Decomposition (POD) to Design Decomposition Methods, Ph.D. thesis, Stanford University, 2006.
- [29] P. Astrid, S. Weiland, K. Willcox, T. Backx, Missing point estimation in models described by proper orthogonal decomposition, *IEEE Transactions on Automatic Control* 53 (2008) 2237–2251.
- [30] R. Bos, X. Bombois, P. Van den Hof, Accelerating large-scale non-linear models for monitoring and control using spatial and temporal correlations, in: *Proceedings of the American Control Conference*, volume 4, pp. 3705–3710.
- [31] S. Chaturantabut, D. C. Sorensen, Nonlinear model reduction via discrete empirical interpolation, *SIAM Journal on Scientific Computing* 32 (2010) 2737–2764.
- [32] D. Galbally, K. Fidkowski, K. Willcox, O. Ghattas, Non-linear model reduction for uncertainty quantification in large-scale inverse problems, *International Journal for Numerical Methods in Engineering* (2009).
- [33] M. Drohmann, B. Haasdonk, M. Ohlberger, Reduced basis approximation for nonlinear parameterized evolution equations based on empirical operator interpolation, *SIAM Journal on Scientific Computing* (2012).
- [34] R. Everson, L. Sirovich, Karhunen–Loève procedure for gappy data, *Journal of the Optical Society of America A* (1995) 1657–1664.
- [35] S. Chaturantabut, D. Sorensen, A state space error estimate for POD–DEIM nonlinear model reduction, Technical Report, Rice University, 2010.
- [36] M. Drohmann, B. Haasdonk, M. Ohlberger, Reduced basis method for finite volume approximation of evolution equations on parametrized geometries, in: *Proceedings of ALGORITHMY*, pp. 1–10.
- [37] N. C. Nguyen, A. T. Patera, J. Peraire, A ‘best points’ interpolation method for efficient approximation of parametrized functions, *International Journal for Numerical Methods in Engineering* 73 (2008) 521–543.
- [38] K. Willcox, Unsteady flow sensing and estimation via the gappy proper orthogonal decomposition, *Computers and Fluids* 35 (2006) 208–226.
- [39] M. Drohmann, B. Haasdonk, M. Ohlberger, Reduced basis model reduction of parametrized two-phase flow in porous media, in: *Proceedings of 7th Vienna International Conference on Mathematical Modelling*.
- [40] P. Astrid, Reduction of Process Simulation Models: A Proper Orthogonal Decomposition Approach, Ph.D. thesis, Technische Universiteit Eindhoven, 2004.

- [41] S. R. Ahmed, G. Ramm, G. Faitin, Some salient features of the time-averaged ground vehicle wake, SAE Paper 840300 (1984).
- [42] P. Geuzaine, G. Brown, C. Harris, C. Farhat, Aeroelastic dynamic analysis of a full F-16 configuration for various flight conditions, AIAA Journal 41 (2003) 363–371.
- [43] C. Farhat, P. Geuzaine, G. Brown, Application of a three-field nonlinear fluid-structure formulation to the prediction of the aeroelastic parameters of an F-16 fighter, Computers & Fluids 32 (2003) 3–29.
- [44] L. Blackford, A. Cleary, J. Choi, E. d’Azevedo, J. Demmel, I. Dhillon, J. Dongarra, S. Hammarling, G. Henry, A. Petitet, et al., ScaLAPACK Users’ Guide, Society for Industrial and Applied Mathematics, 1997.
- [45] C. Hinterberger, M. Garcia-Villalba, W. Rodi, Large eddy simulation of flow around the Ahmed body, in: J. R. R. McCallen, F. Browand (Ed.), The Aerodynamics of Heavy Vehicles: Trucks, Buses, and Trains, Lecture Notes in Applied and Computational Mechanics, volume 19, Springer, 2004.
- [46] K. Carlberg, Model Reduction of Nonlinear Mechanical Systems via Optimal Projection and Tensor Approximation, Ph.D. thesis, Stanford University, 2011.
- [47] J. Nocedal, S. J. Wright, Numerical Optimization, Springer, 2nd edition, 2006.